International Journal of *Molecular Sciences*

*Article*

# Superparamagnetic Spinel-Ferrite Nano-Adsorbents Adapted for $Hg^{2+}$, $Dy^{3+}$, $Tb^{3+}$ Removal/Recycling: Synthesis, Characterization, and Assessment of Toxicity

**A. F. P. Allwin Mabes Raj [1,2,3], Maja Bauman [3], Nena Dimitrušev [3,4], Lamiaa M. A. Ali [5], Mélanie Onofre [5], Magali Gary-Bobo [5], Jean-Olivier Durand [6], Aleksandra Lobnik [3,4] and Aljoša Košak [4,*]**

1 Jožef Stefan International Postgraduate School, Jamova 39, 1000 Ljubljana, Slovenia; allwinamc10@gmail.com
2 Department of Environmental Science, Jožef Stefan Institute, Jamova 39, 1000 Ljubljana, Slovenia
3 Institute for Environmental Protection and Sensors (IOS) Ltd., Beloruska 7, 2000 Maribor, Slovenia
4 Faculty for Mechanical Engineering, University of Maribor, Smetanova 17, 2000 Maribor, Slovenia
5 IBMM, Univ Montpellier, CNRS, ENSCM, 34293 Montpellier, France
6 ICGM, Univ Montpellier, CNRS, ENSCM, 34293 Montpellier, France
* Correspondence: aljosa.kosak@um.si

**Abstract:** In the present work, superparamagnetic adsorbents based on 3-aminopropyltrimethoxy silane (APTMS)-coated maghemite ($\gamma Fe_2O_3@SiO_2–NH_2$) and cobalt ferrite ($CoFe_2O_4@SiO_2–NH_2$) nanoparticles were prepared and characterized using transmission-electron microscopy (TEM/HRTEM/EDXS), Fourier-transform infrared spectroscopy (FTIR), specific surface-area measurements (BET), zeta potential (ζ) measurements, thermogravimetric analysis (TGA), and magnetometry (VSM). The adsorption of $Dy^{3+}$, $Tb^{3+}$, and $Hg^{2+}$ ions onto adsorbent surfaces in model salt solutions was tested. The adsorption was evaluated in terms of adsorption efficiency (%), adsorption capacity (mg/g), and desorption efficiency (%) based on the results of inductively coupled plasma optical emission spectrometry (ICP-OES). Both adsorbents, $\gamma Fe_2O_3@SiO_2–NH_2$ and $CoFe_2O_4@SiO_2–NH_2$, showed high adsorption efficiency toward $Dy^{3+}$, $Tb^{3+}$, and $Hg^{2+}$ ions, ranging from 83% to 98%, while the adsorption capacity reached the following values of $Dy^{3+}$, $Tb^{3+}$, and $Hg^{2+}$, in descending order: Tb (4.7 mg/g) > Dy (4.0 mg/g) > Hg (2.1 mg/g) for $\gamma Fe_2O_3@SiO_2–NH_2$; and Tb (6.2 mg/g) > Dy (4.7 mg/g) > Hg (1.2 mg/g) for $CoFe_2O_4@SiO_2–NH_2$. The results of the desorption with 100% of the desorbed $Dy^{3+}$, $Tb^{3+}$, and $Hg^{2+}$ ions in an acidic medium indicated the reusability of both adsorbents. A cytotoxicity assessment of the adsorbents on human-skeletal-muscle derived cells (SKMDCs), human fibroblasts, murine macrophage cells (RAW264.7), and human-umbilical-vein endothelial cells (HUVECs) was conducted. The survival, mortality, and hatching percentages of zebrafish embryos were monitored. All the nanoparticles showed no toxicity in the zebrafish embryos until 96 hpf, even at a high concentration of 500 mg/L.

**Keywords:** nanomaterials; iron oxides; maghemite; cobalt ferrite; adsorption; transition metals; cytotoxicity; terbium; dysprosium; mercury



**Citation:** Allwin Mabes Raj, A.F.P.; Bauman, M.; Dimitrušev, N.; Ali, L.M.A.; Onofre, M.; Gary-Bobo, M.; Durand, J.-O.; Lobnik, A.; Košak, A. Superparamagnetic Spinel-Ferrite Nano-Adsorbents Adapted for $Hg^{2+}$, $Dy^{3+}$, $Tb^{3+}$ Removal/Recycling: Synthesis, Characterization, and Assessment of Toxicity. *Int. J. Mol. Sci.* **2023**, *24*, 72. https://doi.org/10.3390/ijms241210072

Academic Editor: Gangho Lee

Received: 4 April 2023
Revised: 22 May 2023
Accepted: 26 May 2023
Published: 13 June 2023



## 1. Introduction

Transition metals (TM) and internal transition metals (ITM), often referred to as d- and f-block elements, respectively, are key raw materials for the European economy, forming a strong industrial base that produces a wide range of products and applications used in everyday life and modern technologies. Many of these metals are considered to be highly toxic and have negative environmental and human health effects due to anthropogenic factors (e.g., mercury, lead, chromium, etc.). Furthermore, both groups also include strategic metals, such as rare-earth metals (e.g., dysprosium, terbium, samarium, neodymium, etc.), which are in increasing demand and subject to supply risks. Therefore, reliable and unhindered access to these raw materials is a growing concern in the EU and globally [1–5].

Of these metals, mercury (Hg) is particularly noteworthy. It can be found in many common devices, from thermometers, barometers, thermostats, and pressure gauges to fluorescent lamps, etc., and it is considered to be the most toxic heavy metal in the environment, particularly due to its high bioaccumulation and biomagnification capacity [6]. This is because spilled elemental mercury ($Hg^0$) is converted by microbial processes in the environment, particularly in water, into an organic form called methylmercury (MeHg), which is the most toxic form of mercury. Methylmercury is then transferred to fish and other wildlife and, eventually, it can be ingested, causing adverse health effects [6,7].

The removal of toxic metals, such as mercury, from the environment plays a significant role in minimizing their environmental and human health effects, while the recycling of essential and precious transition metals, such as platinum, palladium, gold, silver, rhodium, iridium, ruthenium, cobalt, niobium, tungsten, etc., and rare-earth metals, such as terbium, dysprosium, neodymium, lanthanum, samarium, cerium, etc., from e-waste and other raw waste materials, is of major importance to increase the availability of secondary resources, as well as improving the knowledge base that provides prerequisites for a circular economy on a larger scale than today [1,6,8–10]. Generally, current processing/removal technologies include, but are not limited to, hydrometallurgy (solvent extraction, ion exchange, precipitation, and crystallization), pyrometallurgy, electrometallurgy (electrorefining, and electrowinning), and aeriometallurgy (supercritical fluid extraction) [11,12].

All these technologies have many disadvantages. Pyrometallurgy is energy-intensive and generates greenhouse gas (GHG) emissions, while hydrometallurgy relies on large volumes of acids and organic solvents, thus generating hazardous wastes [13–15]. The primary disadvantage of aeriometallurgy is that the extraction must be operated at the high pressure (1000–5000 psi) required to maintain the solvent in a supercritical state using supercritical $CO_2$ [16]. In electrometallurgy, an inert atmosphere is usually required for recycling related to operational and maintenance drawbacks, while the recycling of raw metals can generate a small volume of waste, which is not yet developed, qualified, certified, or accepted. However, the electrometallurgy process also features the drawbacks of huge energy consumption for heating and electrolytic reduction and potential chlorine-gas emission [17,18].

An attractive alternative to these technologies is the solid-phase extraction (SPE) of metal ions from the solution using nanostructured materials as adsorbents, characterized by surface functionality, high surface-to-volume ratio, and/or porosity [19,20]. The use of SPE involves the adsorption of the target-metal ions from the solution onto the adsorbent surface followed by the subsequent recycling of the metals and the regeneration of the adsorbents [21,22]. The advantages of SPE include its low solvent consumption, ease of use, efficient removal of metal ions, even at low concentrations, and automation capabilities.

In the last decade, ferrimagnetic iron-oxide nanoparticles (NPs) have received special attention in the field of adsorbents, as reported in many reviews [23–26]. Magnetite ($Fe_3O_4$) and maghemite ($\gamma Fe_2O_3$) are the main types of ferrimagnetic NP, and so far, they have received considerable attention due to their nontoxicity and biocompatibility [27–29], as well as their ability to be easily dispersed and collected using an external magnetic field [30–32]. These ferrimagnetic materials, when reduced to particle dimensions smaller than a certain domain, exhibit superparamagnetic behavior, which means that when an external magnetic field is applied, they magnetize to saturation magnetization ($\sigma_s$), but when the magnetic field is removed, they no longer exhibit either residual magnetism ($M_r$) or coercivity ($H_c$) [33]. Hence, superparamagnetic iron-oxide NPs can be easily guided in the magnetic field [25,27,34,35]. One prominent example is the introduction of cobalt ($Co^{2+}$) ions into an iron-oxide spinel crystal lattice. Cobalt-doped iron oxides, also known as cobalt ferrites ($CoFe_2O_4$), arouse interest in adsorption applications as their magnetocrystalline anisotropy, which affects the magnetization, coercivity, reversal, and relaxation of nanoparticles, can be tuned by the substitution of cobalt for iron [36–40].

Due to the increasing use of iron-oxide NPs as adsorbents in the recycling of strategic transition metals, there is a high likelihood that these NPs may ultimately enter aquatic ecosystems through effluent discharge and leaching during or after recycling activities, thereby affecting the environment and human health. Unfortunately, there is a serious lack of accurate and sufficient information on their toxic effects. Therefore, toxicity assessment has become increasingly important to understand the impact of these NPs on human health and the environment [41].

In many studies, it was found that uncoated NPs usually tend to be more toxic than coated particles; therefore, the surface modification of uncoated NPs can significantly reduce their toxicity [41–49]. Other studies revealed significant cytotoxic effects of these NPs, such as inflammation, the formation of apoptotic bodies, impaired mitochondrial function (MTT), the leakage of membrane lactate dehydrogenase (LDH assay), the generation of reactive oxygen species (ROS), increases in the number of micronuclei as indicators of gross chromosomal damage (a measure of genotoxicity), and chromosome condensation [44,48,50–54].

Furthermore, little is known about the toxicity of the metal dopants of iron-oxide NPs such as cobalt ($Co^{2+}$). The potential toxicity of cobalt-doped iron oxide ($CoFe_2O_4$) is therefore the subject of many debates concerning environmental, health, and safety issues, particularly their use in the environment and their effects on human health [28,44,55–62].

One of the simplest ways to modify the surfaces of NPs is to use alkoxysilanes, which are considered among the preferred coating materials due to their chemical stability, biocompatibility [63–65], and versatility, to achieve the functionality [65,66] required in the end-use applications of NPs.

To ensure the functionality of iron-oxide NPs, various alkoxysilane ligands can be grafted directly to their surfaces in one step, avoiding an intermediate multistage reaction mechanism. The grafting principle of alkoxysilanes is based on the sol-gel hydrolysis of alkoxide groups in the structures of alkoxysilane precursors, producing silanol groups (Si-OH), which undergo condensation reactions to form siloxane bonds (Si–O–Si) on the surface of the iron oxide, resulting in the formation of a protective silica surface layer ($SiO_2$). Many alkoxysilanes may contain various functional groups in their aliphatic chains, such as hydroxyl (–OH), amine (–$NH_2$), mercapto (–SH), carboxylic (–COOH), sulphonic (–$SO_3H$), phosphonate (–$PO(OH)_2$), phosphate (–$PO_2(OH)_2$), etc., which contain electron-donor atoms (O, N, P, S) and allow the formation of relatively strong complexes with the target transition-metal ions to be recycled [31,41,42,45,67–71].

Although many studies report that alkoxysilanes are non-toxic [18–20,71–73], their toxicity in terms of reactivity, stability, and degradation effects has not yet been thoroughly investigated [74–77].

In the present work, we attempted to fabricate efficient superparamagnetic adsorbents based on two different spinel-type iron oxides, both maghemite ($\gamma Fe_2O_3$) and cobalt ferrite ($CoFe_2O_4$), which were surface-functionalized using a (3-aminopropyl)trimethoxy silane (APTMS) precursor. The functionalized superparamagnetic adsorbents were characterized to test their adsorption efficiency and adsorption capacity towards $Dy^{3+}$, $Tb^{3+}$, and $Hg^{2+}$ ions in aqueous solutions and their desorption efficiency when an acidic medium was used. The assessment of the cytotoxicity of both types of NP with and without an amino-propyl (–$(CH_2)_3NH_2$) surface coating was conducted on four different types of healthy cell: human-skeletal-muscle-derived cells, human fibroblasts, murine macrophages cells, and human-umbilical-vein endothelial cells. Further, their toxic effects on zebrafish embryos were also evaluated by recording the survival, mortality, and hatching percentages during embryo development.

## 2. Results and Discussion

### *2.1. Synthesis and Characterization of MNPs*

The magnetic $\gamma Fe_2O_3$ and $CoFe_2O_4$ NPs prepared by the coprecipitation method were characterized using XRD (Figure 1). All the diffraction peaks of the prepared samples were consistent with the cubic spinel crystal structure (JCPDS Card 39-1346). It can be seen from the XRD pattern that the presence of diffraction lines at $2\theta$ of 30.5°, 35.5°, 43.2°, 53.6°, 57.1°, and 62.9° for both samples corresponded to the cubic crystal planes of (220), (311), (400), (422), (511), and (440), respectively. The particle sizes of the $\gamma Fe_2O_3$ and $CoFe_2O_4$ were calculated from the broadening of the most intensive diffraction peak corresponding to the (311) crystal plane using the Deby–Scherrer equation [78,79]. The calculated average particle sizes of the $\gamma Fe_2O_3$ and $CoFe_2O_4$ were 10.2 nm and 11.5 nm, respectively, and the crystalline-lattice parameters corresponding to the cubic spinel crystal structure obtained based on Bragg's law were 0.8358 nm and 0.8345 nm, respectively. The presence of broad amorphous diffraction peaks for the functionalized $\gamma Fe_2O_3@SiO_2–NH_2$ and $CoFe_2O_4@SiO_2–NH_2$ NPs, which appeared at a low diffraction angle 2$\theta$ of 20°, was due to the presence of the amorphous $SiO_2$ surface layer, indicating that the crystalline cubic spinel $\gamma$-$Fe_2O_3$ and $CoFe_2O_4$ NPs were successfully surface-functionalized with APTMS [80].

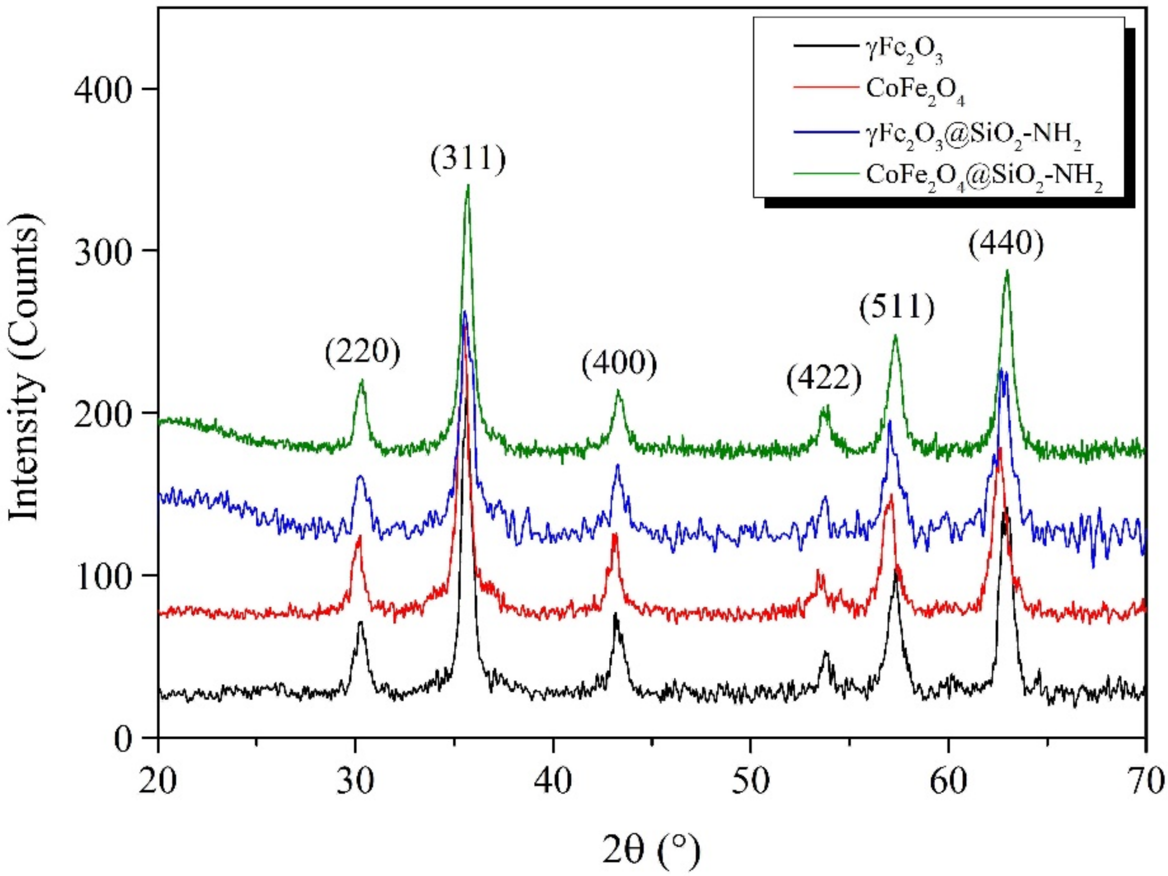


**Figure 1.** XRD patterns of $\gamma Fe_2O_3$ and $CoFe_2O_4$ NPs.

The positions of the diffraction peaks for the $\gamma Fe_2O_3@SiO_2–NH_2$ and $CoFe_2O_4@SiO_2$-$NH_2$ NPs were at the same positions 2$\theta$ as those of the $\gamma Fe_2O_3$ and $CoFe_2O_4$, indicating that the crystalline cubic spinel structures remained unchanged after their functionalization with APTMS.

The transmission-electron micrographs in Figure 2 represent the morphological properties of the as-prepared $\gamma Fe_2O_3$ and $CoFe_2O_4$ NPs and functionalized $Fe_2O_3@SiO_2–NH_2$ and $CoFe_2O_4@SiO_2–NH_2$ core@shell nanostructures. It can be seen that the obtained $\gamma Fe_2O_3$ and $CoFe_2O_4$ NPs were relatively spherical in shape, with average particle sizes of (9.9 $\pm$ 0.9) nm and (11.5 $\pm$ 1.0) nm, respectively, while the particle-size distributions of the functionalized $\gamma Fe_2O_3@SiO_2–NH_2$ and $CoFe_2O_4@SiO_2–NH_2$ NPs were (14.5 $\pm$ 1.1) nm and (17.7 $\pm$ 1.2) nm, respectively. The electron-diffraction patterns of the $\gamma Fe_2O_3$ and $CoFe_2O_4$ NPs indicated the crystalline nature of the prepared powders, with each of the concentric diffraction rings belonging to the spinel crystal structure.

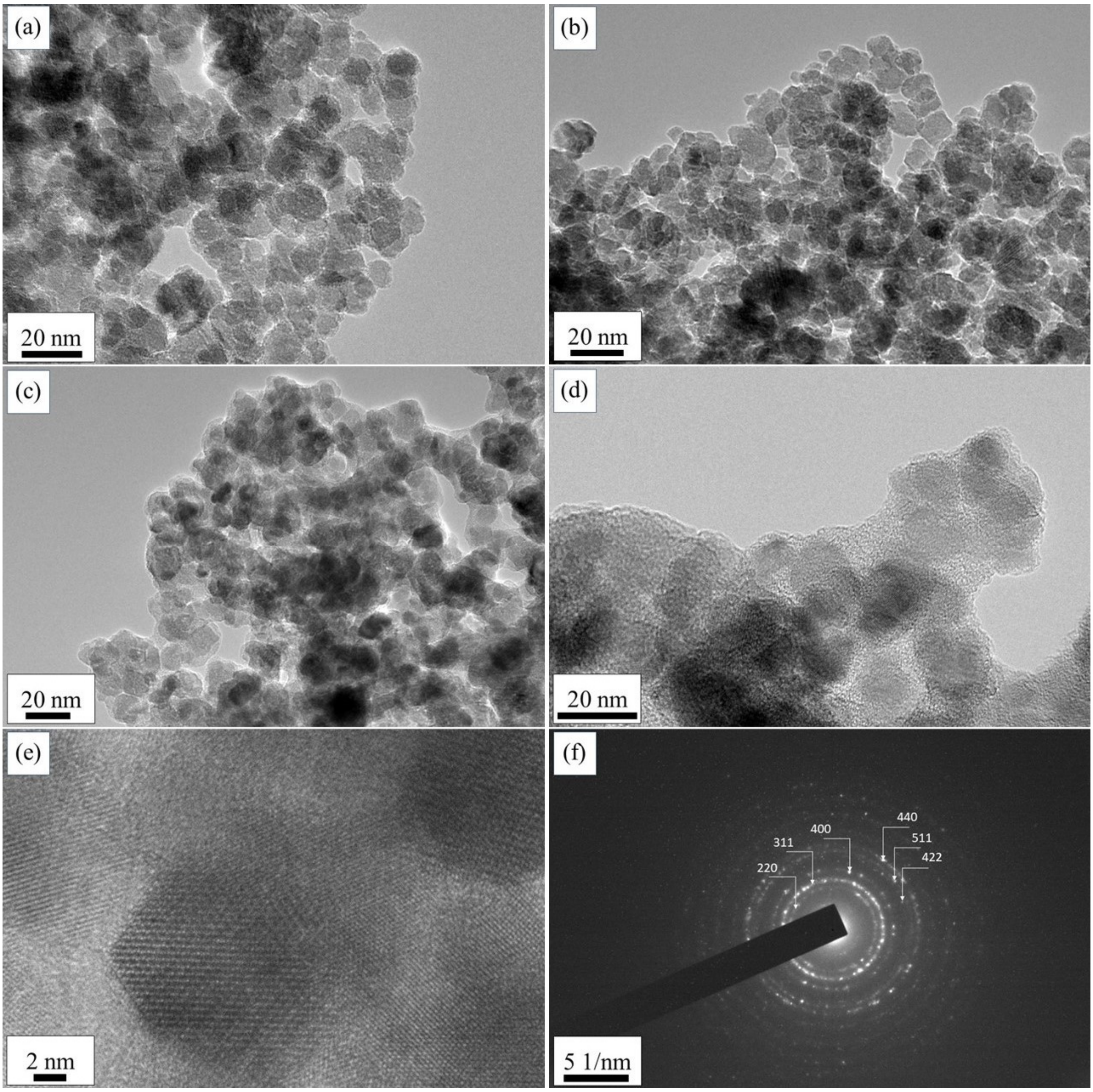


**Figure 2.** TEM micrographs of (**a**) $\gamma Fe_2O_3$, (**b**) $CoFe_2O_4$, (**c**) $\gamma Fe_2O_3@SiO_2–NH_2$, (**d**) $CoFe_2O_4@SiO_2–NH_2$, (**e**) high-resolution image (HRTEM), and (**f**) electron-diffraction pattern of spinel $\gamma Fe_2O_3$ and $CoFe_2O_4$ NPs.

The EDXS patterns of the $\gamma Fe_2O_3$ and $CoFe_2O_4$ NPs in Figure 3a,b confirm the presence of Co, Fe, and O elements, indicating the formation of $\gamma Fe_2O_3$ and $CoFe_2O_4$ nanostructures, while on the EDXS spectrum of the $\gamma Fe_2O_3@SiO_2–NH_2$ and $CoFe_2O_4@SiO_2–NH_2$ in Figure 3c,d, respectively, the presence of C, O(N), Co, Fe, and Si confirmed the success of the surface functionalization of the $\gamma Fe_2O_3$ and $CoFe_2O_4$ NPs with APTMS and, thus, the formation of the core@shell nanostructures. Small proportions of Cu and C elements belong to the TEM copper-grid supported transparent carbon foil.

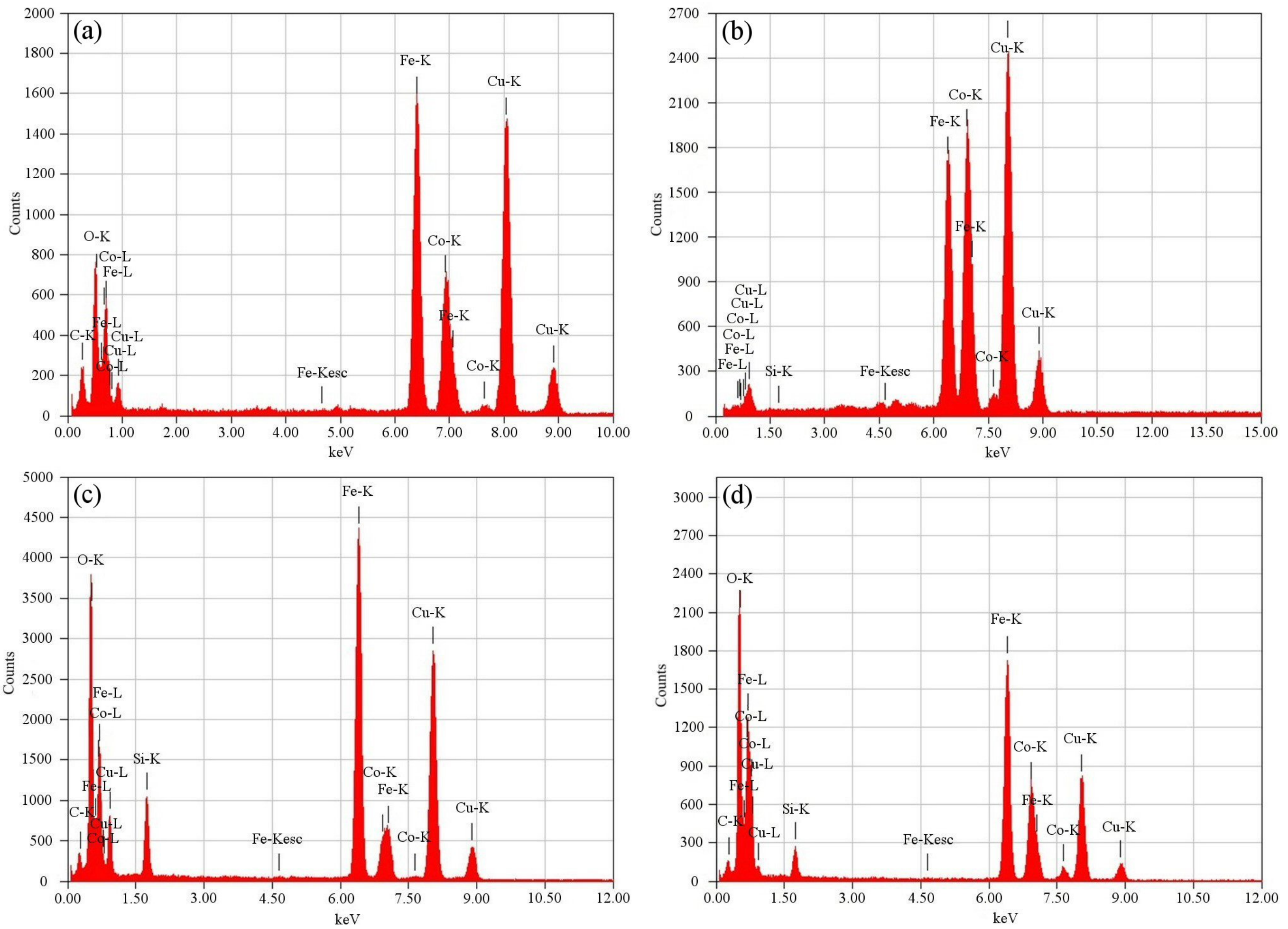


**Figure 3.** EDXS spectra of (**a**) $\gamma Fe_2O_3$, (**b**) $CoFe_2O_4$, (**c**) $\gamma Fe_2O_3$@$SiO_2$–$NH_2$, and (**d**) $CoFe_2O_4$@$SiO_2$–$NH_2$ NPs.

The Brunauer–Emmet–Teller (BET) analysis showed specific surface areas of 94.9 $m^2/g$ for the $\gamma Fe_2O_3$ and 62.5 $m^2/g$ for the $CoFe_2O_4$. According to the BET-specific surface area at a relative pressure of 0.3, average particle sizes ($d_{bet}$) of 15.1 nm and 18.5 nm were calculated for the $\gamma Fe_2O_3$ and $CoFe_2O_4$, respectively, assuming the sphericity of the NPs using the equation $S_{bet} = 6/(d_{bet} \cdot \rho)$, where $\rho$ is a theoretical density of 4.9 $g/cm^3$ for $\gamma Fe_2O_3$ [81] and 5.2 $g/cm^3$ for $CoFe_2O_4$ [82]. The average size calculated from the surface area was a little higher than that determined using the XRD, most probably due to the agglomeration of the particles [83]. For the Barrett–Joyner–Halenda (BJH) adsorption, the average pore size was 7.0 nm, with a total pore volume of 0.2335 $cm^3/g$, for the $\gamma Fe_2O_3$ NPs, and 5.8 nm, with a total pore volume of 0.1275 $cm^3/g$, for the $CoFe_2O_4$ NPs. Furthermore, for the BJH desorption, the average pore size was 8.4 nm, with a total pore volume of 0.3152 $cm^3/g$, for the $\gamma Fe_2O_3$, and 6.1 nm, with a total pore volume of 0.1353 $cm^3/g$, for the $CoFe_2O_4$ NPs.

Due to the surface functionalization of the $\gamma Fe_2O_3$ and $CoFe_2O_4$ NPs with APTMS, the obtained specific surface area decreased to 40.5 $m^2/g$ for the $\gamma Fe_2O_3$@$SiO_2$–$NH_2$ and 44.7 $m^2/g$ for the $CoFe_2O_4$@$SiO_2$–$NH_2$. It is known that the larger the surface area, the smaller the particle size, and a smaller BET surface area means a larger particle size. According to the specific surface areas, the average particle sizes of the prepared $\gamma Fe_2O_3$@$SiO_2$–$NH_2$ and $CoFe_2O_4$@$SiO_2$–$NH_2$ samples were calculated as 30.2 nm and 25.8 nm, respectively.

A FTIR analysis (Figure 4) was performed to obtain additional information on the coverage of the NPs with the APTMS.

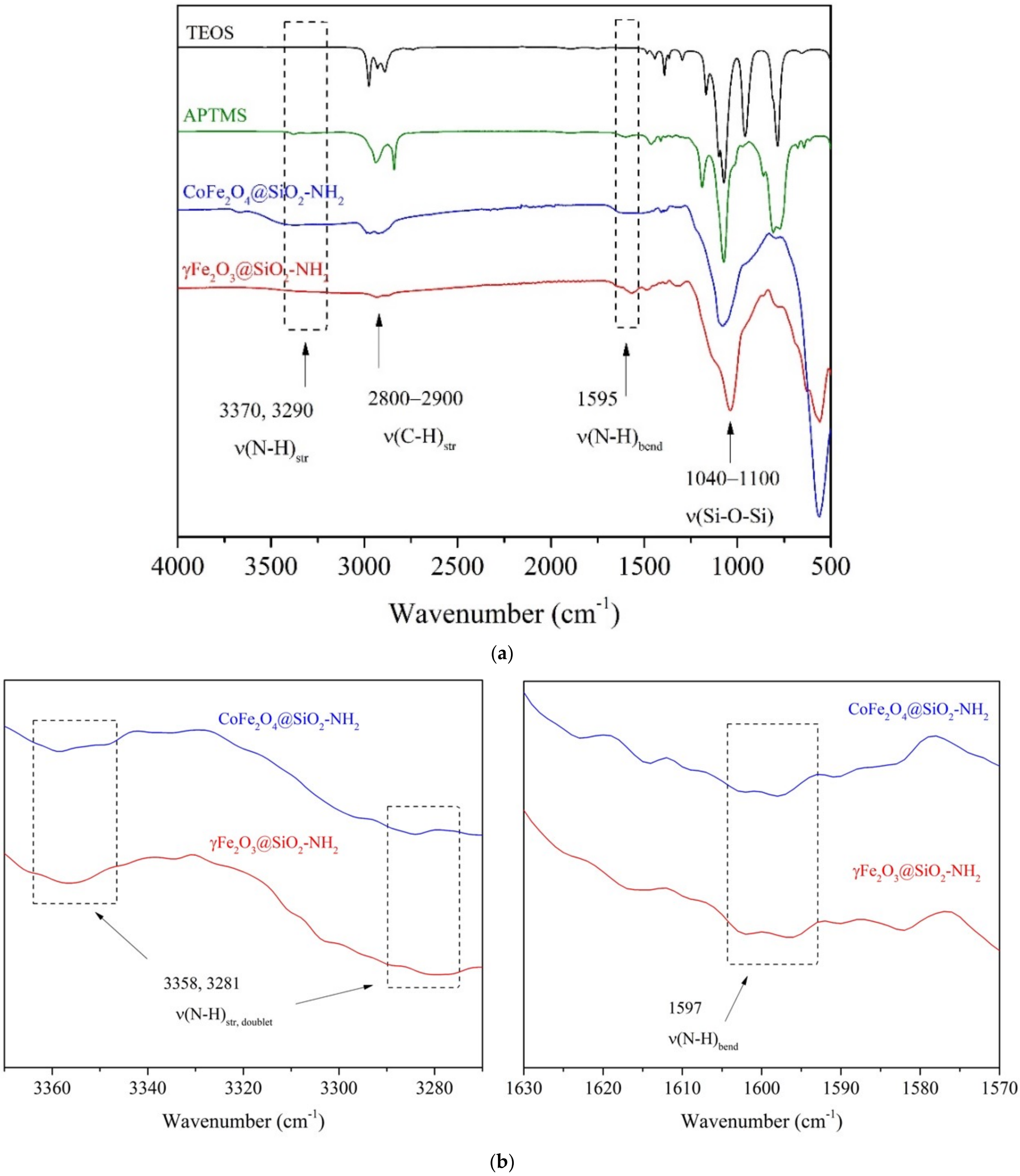


**Figure 4.** (**a**) FTIR spectra of as-prepared $\gamma Fe_2O_3@SiO_2–NH_2$ and $CoFe_2O_4@SiO_2–NH_2$ NPs and pure alkoxide precursors TEOS and APTMS, and (**b**) enlarged area corresponding to vibrations of amino groups.

In the FTIR spectra (Figure 4a), the two peaks near 3400 $cm^{-1}$ and 1630 $cm^{-1}$ were assigned to the hydroxyl group OH for all the synthesized NPs. The functionalization process of the $\gamma Fe_2O_3$ and $CoFe_2O_4$ NPs with alkoxysilanes was verified by the asymmetric stretching vibrations of the Si-O-Si bonds at 1050 $cm^{-1}$ and the bending of the Si-H bonds at 796 $cm^{-1}$ and at 988 $cm^{-1}$, indicating the formation of silica ($SiO_2$) shells.

The presence of amino-propyl groups in the $\gamma Fe_2O_3@SiO_2–NH_2$ and $CoFe_2O_4@SiO_2–NH_2$ samples was confirmed by the peaks at 2934 $cm^{-1}$, 1615 $cm^{-1}$, 1336 $cm^{-1}$, and 781 $cm^{-1}$, which were assigned to the stretching vibrations of the $–CH_2–NH_2$ bonds, the bending of N–H and $NH_2$, the wagging and twisting of $–CH_2–NH_2$, and the wagging and twisting of primary amino groups ($–NH_2$), respectively. These peaks in the source spectra were not sufficiently visible, but enlarged individual peak areas confirmed their presence (Figure 4b).

A thermogravimetric analysis (Figure S1) was used to determine the thermal stability and the percentage of amino-propyl ligands grafted onto the surface of the magnetic $\gamma Fe_2O_3$ and $CoFe_2O_4$ NPs. According to the literature, the estimation of mass-loss values of 1.1% and 1.3% (not shown in Figure 5) while heating as-prepared magnetic $\gamma Fe_2O_3$ and $CoFe_2O_4$ NPs up to 200 °C usually corresponds to the evaporation of physically and chemically absorbed moisture. Further heating of the $\gamma Fe_2O_3$ and $CoFe_2O_4$ magnetic NPs up to 900 °C, respectively, resulted in additional mass losses of 2.7% and 3.4%, respectively, which were most likely due to phase and surface changes, the reduction in porosity, and the degradation of the remaining surface species.

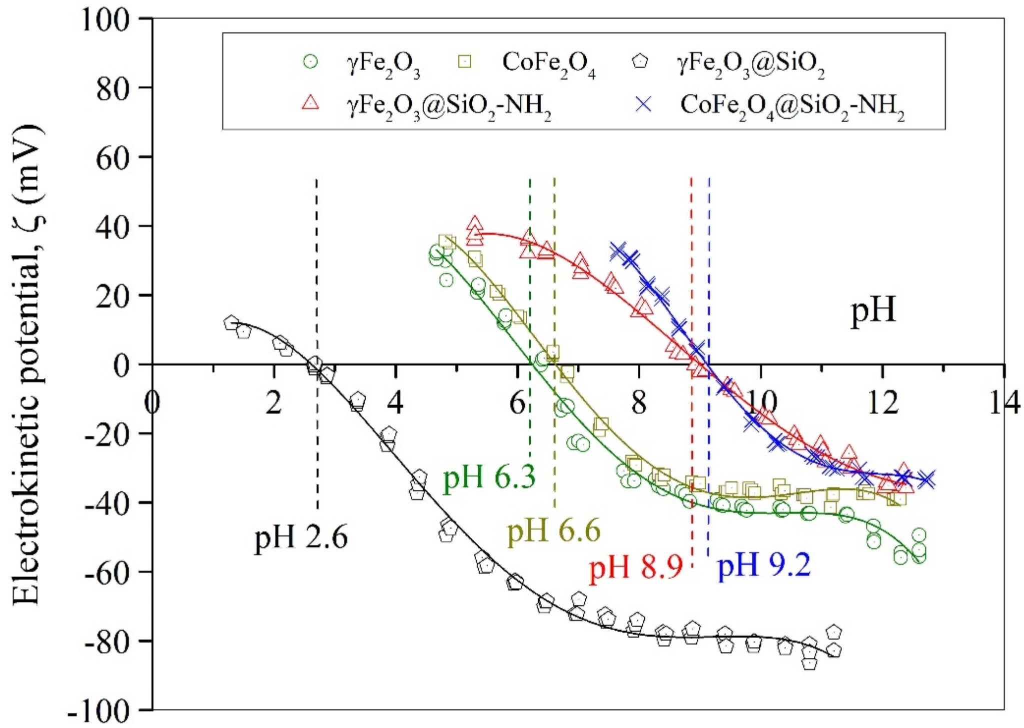


**Figure 5.** The electrokinetic (ζ) potential of the prepared NPs.

The mass losses of the prepared $\gamma Fe_2O_3@SiO_2–NH_2$ and $CoFe_2O_4@SiO_2–NH_2$ samples of 3.1% and 1.8%, respectively (not shown in Figure S1), began at the initial 30 °C mark and continued evolving up to 150 °C. These changes were related to the evaporation of the absorbed moisture from their structures. Further heating of the $\gamma Fe_2O_3@SiO_2–NH_2$ and $CoFe_2O_4@SiO_2–NH_2$ samples up to 900 °C caused more remarkable mass losses of 21.5% and 20.1%, respectively, which corresponded to the decomposition of the $SiO_2$ shell and the removal of amino-propyl groups from the NP surfaces, followed by the reduction in the porosity and the cracking of the residual siloxane species, Si–O–Si.

To establish the stability of the prepared $\gamma Fe_2O_3$, $CoFe_2O_4$, $\gamma Fe_2O_3@SiO_2–NH_2$, and $CoFe_2O_4@SiO_2–NH_2$ NPs in an aqueous medium and to determine their surface potential and isoelectric points (IEP), the electrokinetic (ζ) potential as a function of pH media was measured (Figure 5). The pH values of the IEPs for the $\gamma Fe_2O_3$ and $CoFe_2O_4$ NPs were about 6.3 and 6.6, respectively, while the silica-coated NPs showed pH dependencies similar to that of pure silica, i.e., at pH 2–3 [69,84].

The values of the ζ-potential for the $\gamma Fe_2O_3$ and $CoFe_2O_4$ NPs were higher than +30 mV at pH < 5.2 and lower than −30 mV at pH > 7.9, which means that the $\gamma Fe_2O_3$ and $CoFe_2O_4$ NPs were stable in the aqueous media at pH smaller than 5.2 and higher than 7.9. In that pH range, the electrostatic repulsions between the NPs dispersed in an aqueous medium are stronger than the random thermal Brownian motion and, therefore, prevent them from accidental collision and agglomeration and, subsequently, from settling out.

The observed IEP at pH 2.4 for the $\gamma Fe_2O_3@SiO_2$ NPs confirmed that the silica-coating process of the $\gamma Fe_2O_3$ NPs was effective, since the charged surface properties were close to those of pure silica (i.e., at pH 2–3) [84]. The silica shell at the maghemite cores caused an increase in their chemical stability at pH values > 4.1, where the surface potential was lower than −30 mV, thus rendering their performance suitable for environmental applications. Moreover, the silica coating prevented the dissolution of the $\gamma Fe_2O_3$ and $CoFe_2O_4$ NPs and, thus the leaching of potentially toxic $Co^{2+}$ ions from the spinel crystalline structure and the $Fe^{2+}/Fe^{3+}$ oxidation, which otherwise occurs in an acidic medium at values of pH < 3.

It can be seen that an APTMS precursor may be employed to functionalize $\gamma Fe_2O_3$ and $CoFe_2O_4$ NPs to form functional $\gamma Fe_2O_3@SiO_2–NH_2$ and $CoFe_2O_4@SiO_2–NH_2$ core@shell nanostructures. The presence of an amine layer on the surface of the $\gamma Fe_2O_3@SiO_2–NH_2$ and $CoFe_2O_4@SiO_2–NH_2$ NPs makes them positive in a broad range of pH due to the protonation and deprotonation of the amine groups, which depend on the solution's pH values.

The zeta (ζ) potential measurement of the $\gamma Fe_2O_3@SiO_2–NH_2$ and $CoFe_2O_4@SiO_2–NH_2$ NPs in an aqueous solution showed an isoelectric point at about pH 9.0 and stability of the NPs at pH < 6.6 for the $\gamma Fe_2O_3@SiO_2$-$NH_2$ and at pH < 7.9 for the $CoFe_2O_4@SiO_2–NH_2$, where the ζ–potential was higher than +30 mV, and at pH > 10.6, where the ζ–potential was lower than −30 mV.

We used pH potentiometric titrations for the determination of the total charge of the aqueous colloidal dispersions of the $\gamma Fe_2O_3@SiO_2–NH_2$ and $CoFe_2O_4@SiO_2–NH_2$ NPs.

The results of the potentiometric titration isotherms for the $\gamma Fe_2O_3@SiO_2–NH_2$ and $CoFe_2O_4@SiO_2–NH_2$ NPs are presented in Figure S2. The data exhibited protonation and deprotonation progress for both samples at an alkaline pH of around 10, exhibiting a pKa value of 10.1 for the $\gamma Fe_2O_3@SiO_2–NH_2$ with a maximum charge of 0.0485 mmol/g and a pKa value of 9.9 for the $CoFe_2O_4@SiO_2–NH_2$ with a maximum charge of 0.0155 mmol/g. This can be attributed to the contribution of the total primary amine groups, which is in agreement with data published elsewhere [85,86], and indicates the successful surface functionalization of the MNPs with APTMS.

Figure 6a shows the hydrodynamic size distribution of the aqueous colloidal $\gamma Fe_2O_3$, $CoFe_2O_4$, $\gamma Fe_2O_3@SiO_2–NH_2$, and $CoFe_2O_4@SiO_2–NH_2$ NPs at 21 °C, according to the intensity-distribution pattern, showing a narrow distribution with homogeneous sizes. The $\gamma Fe_2O_3$ and $CoFe_2O_4$ NPs, which were an average diameters of 9.9 nm and 11.5 nm by the TEM, in fact exhibited slightly larger hydrodynamic sizes of approximately 11.7 nm and approximately 14.5 nm, respectively (Figure 6a). On the other hand, after the surface functionalization with the APTMS, the $\gamma Fe_2O_3@SiO_2–NH_2$ and $CoFe_2O_4@SiO_2–NH_2$ NPs showed larger hydrodynamic sizes, of about 16.6 nm and about 19.1 nm, respectively (Figure 6a), compared to the previous primary particle sizes of the same nanoparticles observed by TEM.

It is worth noting that these hydrodynamic sizes were maintained over the applied time range of 1 h (Figure 6a), indicating that both the uncoated $\gamma Fe_2O_3$ and $CoFe_2O_4$ and the surface-functionalized $\gamma Fe_2O_3@SiO_2–NH_2$ and $CoFe_2O_4@SiO_2–NH_2$ NPs retained colloidal stability.

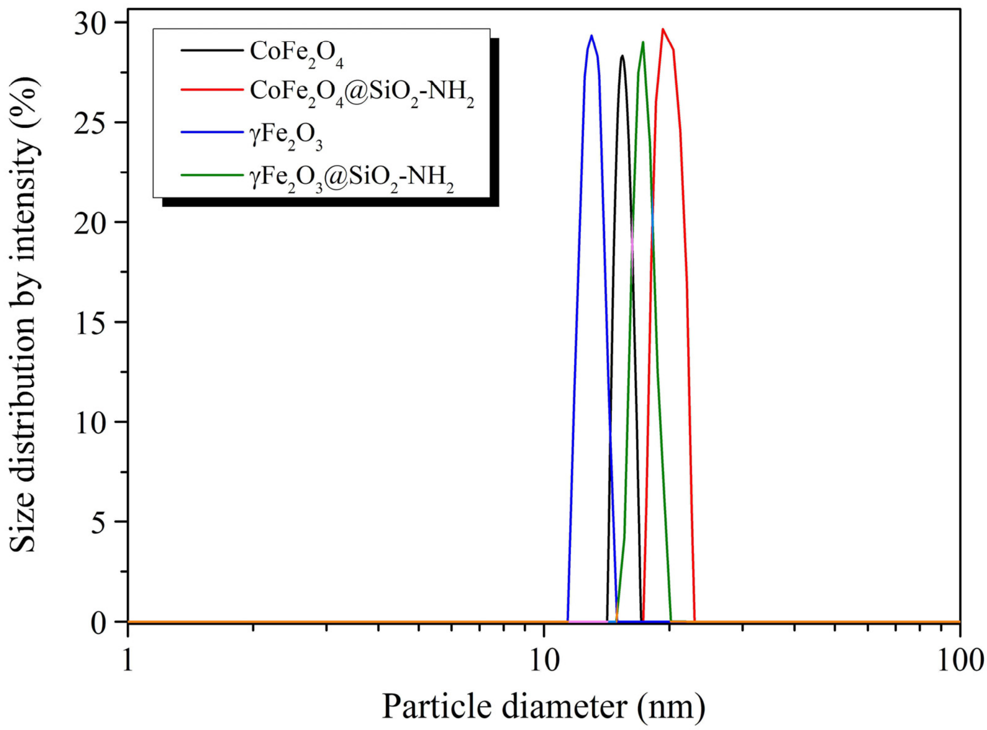


(**a**)

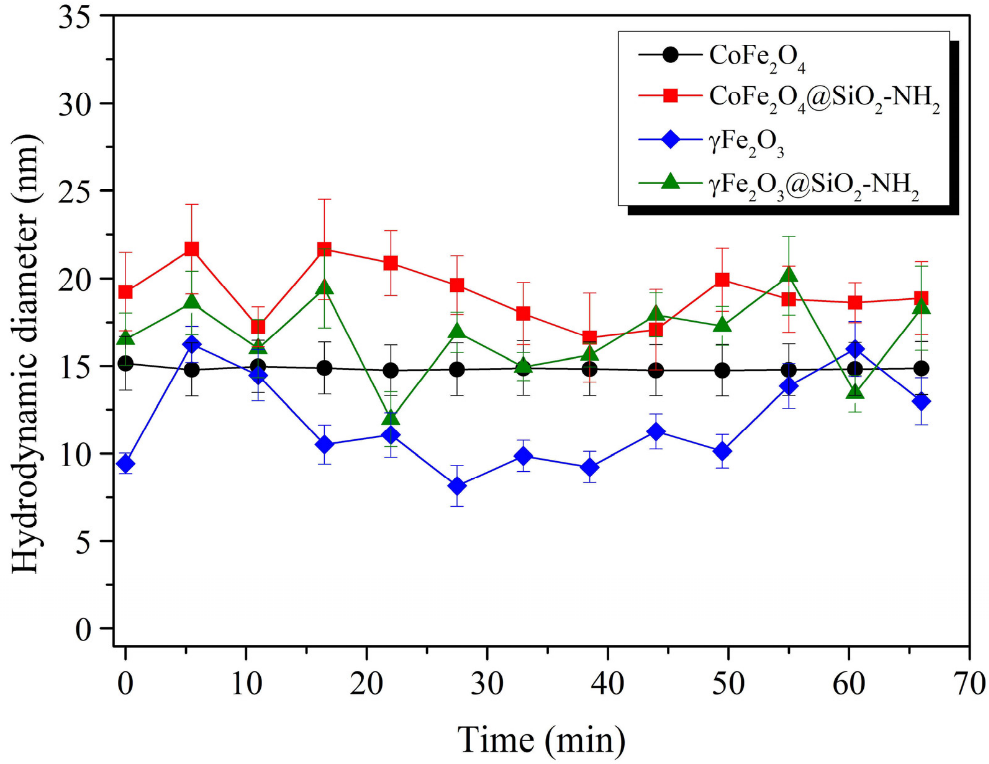


(**b**)

**Figure 6.** (**a**) Hydrodynamic particle-size distribution for $\gamma Fe_2O_3$, $CoFe_2O_4$, $\gamma Fe_2O_3@SiO_2–NH_2$, and $CoFe_2O_4@SiO_2–NH_2$ NPs, and (**b**) the time-dependent hydrodynamic diameters of uncoated $\gamma Fe_2O_3$ and $CoFe_2O_4$, and coated $\gamma Fe_2O_3@SiO_2$-$NH_2$ and $CoFe_2O_4@SiO_2$-$NH_2$ NPs.

The time-dependent hydrodynamic diameters of uncoated $\gamma Fe_2O_3$ and $CoFe_2O_4$, and coated $\gamma Fe_2O_3@SiO_2–NH_2$ and $CoFe_2O_4@SiO_2–NH_2$ NPs, are shown in Figure 6b.

Figure 6b shows the samples showed a trend towards colloidal stability. The hydrodynamic diameter of the colloidal $CoFe_2O_4$ NPs did not change significantly with time. The average hydrodynamic size of the colloidal $CoFe_2O_4$ NPs was maintained at approximately (11.7 ± 1.1) nm over the entire time range. The colloidal $\gamma Fe_2O_3$ NPs also had a similar behavioral pattern in terms of hydrodynamic size, with a slightly larger fluctuation in the values around the average diameter of the NPs of (14.8 ± 1.5) nm. Although the overall maximum average hydrodynamic sizes of the $\gamma Fe_2O_3$ and $CoFe_2O_4$ NPs increased with respect to the particle-size values estimated from the XRD and TEM images, no agglomeration or aggregation of NPs was observed.

After the surface functionalization of the $\gamma Fe_2O_3$ and $CoFe_2O_4$ NPs by the APTMS, a fluctuation and an increase in the hydrodynamic diameters of the $\gamma Fe_2O_3@SiO_2–NH_2$ and $CoFe_2O_4@SiO_2–NH_2$ NPs by about 42% and 30%, respectively, were observed in relation to the uncoated $\gamma Fe_2O_3$ and $CoFe_2O_4$ NPs. The final hydrodynamic sizes of the $\gamma Fe_2O_3@SiO_2–NH_2$ and $CoFe_2O_4@SiO_2–NH_2$ NPs were 16.6 ± 1.5 nm and 19.1 ± 2.0 nm, respectively, compared to the particle-size values estimated from the XRD and TEM images. Despite the fluctuation and increase in the total maximum hydrodynamic sizes of the $\gamma Fe_2O_3@SiO_2–NH_2$ and $CoFe_2O_4@SiO_2–NH_2$ NPs, no agglomeration or aggregation of NPs was observed. The samples showed a trend toward colloidal stability.

It is obvious that the average particle sizes measured by the DLS technique were slightly larger than the average particle sizes estimated on the basis of the XRD and TEM. It is known that the hydrodynamic sizes of particles dispersed in liquids are usually larger than the primary particle sizes, as reported by many other studies [87–90]. The hydrodynamic sizes of particles measured by DLS depend on many factors, particularly the concentration of the dispersion, temperature, pH, etc., due to which dispersed nanoparticles may tend to aggregate; therefore, the measured hydrodynamic diameters in such cases are usually much larger than the actual sizes [88,90].

Figure 7 shows the comparison of the magnetic properties of the uncoated $\gamma Fe_2O_3$ and $CoFe_2O_4$ NPs and the functionalized $\gamma Fe_2O_3@SiO_2–NH_2$ and $CoFe_2O_4@SiO_2–NH_2$ NPs, which were carried out using VSM analysis.

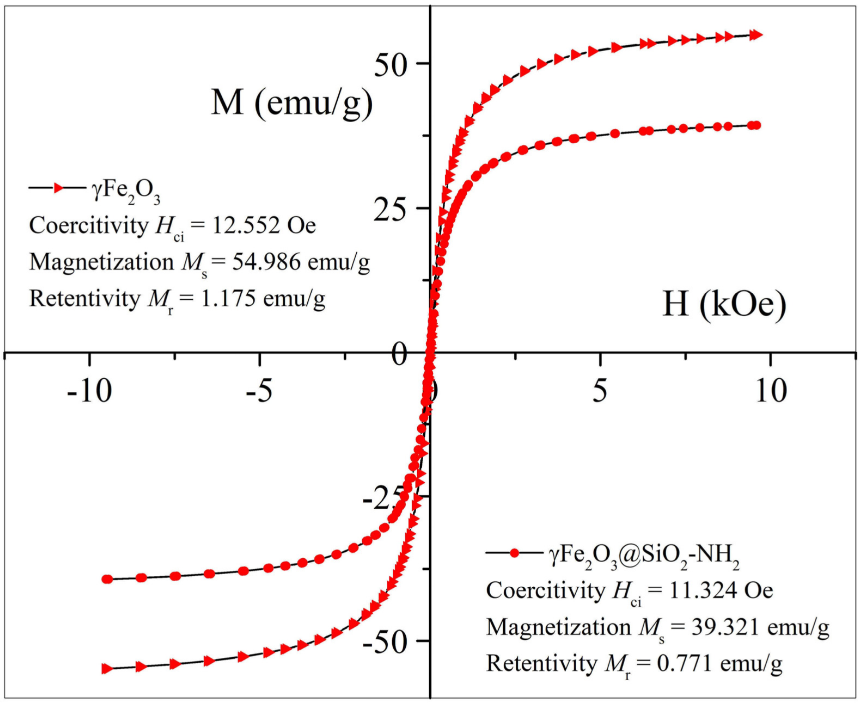


(**a**)

**Figure 7.** *Cont.*

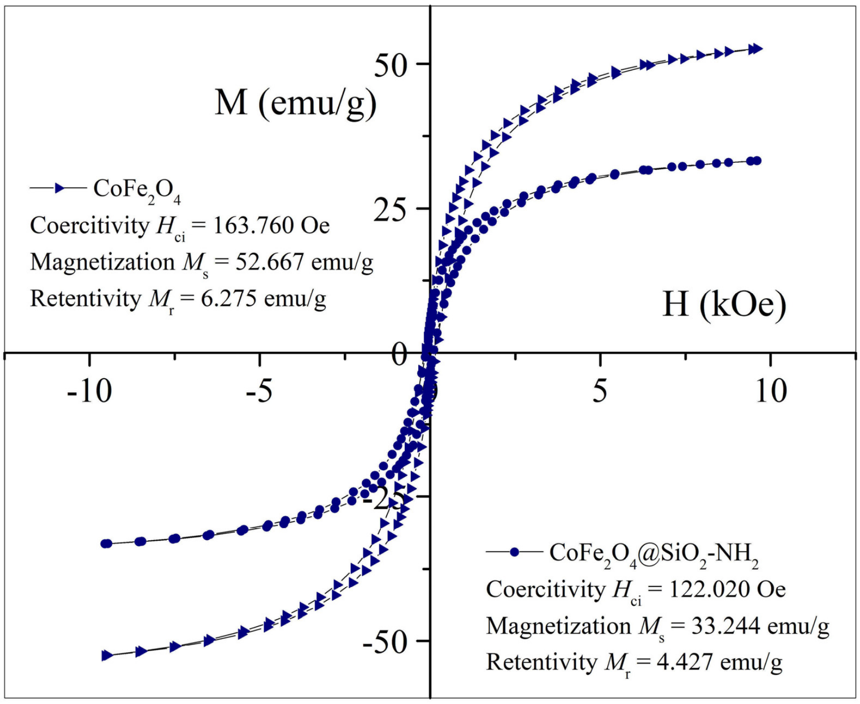


(**b**)

**Figure 7.** *M-H* curves of the prepared samples of (**a**) γ-$Fe_2O_3$ and γ-$Fe_2O_3$@$SiO_2$–$NH_2$ NPs, and (**b**) $CoFe_2O_4$ and $CoFe_2O_4$@$SiO_2$–$NH_2$ NPs.

At the maximum magnetic field (*H*) strength in the magnetization phase, the specific mass magnetization ($M_s$) of the samples γ$Fe_2O_3$ and $CoFe_2O_4$ reached values of 54.98 emu/g and 52.67 emu/g, respectively. The remanent magnetization ($M_r$) and coercivity ($H_{ci}$) values for the samples γ$Fe_2O_3$ and $CoFe_2O_4$ can be determined from the shape of the hysteresis curves in the vicinity of the zero-magnetic-field strength. We determined that the remanent magnetization and coercivity of the γ$Fe_2O_3$ sample were 1.17 emu/g and 12.55 Oe, respectively, and that the remanent magnetization and coercivity of the $CoFe_2O_4$ sample were 6.27 emu/g and 163.76 Oe, respectively.

As can be seen, the γ$Fe_2O_3$ NPs showed very low coercivity due to the small particle sizes. In this case, the γ$Fe_2O_3$ NPs exhibited a superparamagnetic character; in other words, they were monodomain. In contrast, when the iron in the spinel crystal structure of the maghemite (γ$Fe_2O_3$) replaced the cobalt ($CoFe_2O_4$), the coercivity was non-zero, and the samples did not show superparamagnetic behavior.

A comparison of the magnetic characteristics of these two samples showed that with the integration of the cobalt into the γ$Fe_2O_3$ spinel crystal structure, the coercivity increased by thirteen times, and the remanent magnetization increased by almost five times, while the specific mass magnetization did not change significantly.

The increase in coercivity was the cause of the increase in the magnetocrystalline anisotropy due to the cobalt substitution [39]. Magnetocrystalline anisotropy is a key factor that determines the superparamagnetic behavior of nanocrystalline particles and serves as an energy barrier to block spin relaxation, which changes the magnetic state from ferrimagnetic to superparamagnetic [37,38].

The average particle sizes of samples γ$Fe_2O_3$ and $CoFe_2O_4$ were approximately similar (10.2 nm for γ$Fe_2O_3$ and 11.5 nm for $CoFe_2O_4$), so the loss of superparamagnetic properties when replacing the iron with the cobalt in the γ$Fe_2O_3$ spinel crystal structure may have been due to an increase in the magnetocrystalline anisotropy of the $CoFe_2O_4$ [37].

In the magnetization step, under the maximum magnetic field strength ($H_{ci}$), the specific mass magnetization ($M_s$) of the synthesized γ$Fe_2O_3$@$SiO_2$–$NH_2$ decreased from 54.98 emu/g for the γ$Fe_2O_3$ NPs to 39.32 emu/g, and from 52.67 emu/g for the $CoFe_2O_4$

NPs to 33.24 emu/g for the $CoFe_2O_4@SiO_2–NH_2$ NPs. This was due to the presence of a non-magnetic $SiO_2$-$NH_2$ coating on the surfaces of the $\gamma Fe_2O_3$ and $CoFe_2O_4$ cores, which, due to its diamagnetic quality, contributed to the reduction in the net-specific magnetization of the $\gamma Fe_2O_3@SiO_2–NH_2$ and $CoFe_2O_4@SiO_2–NH_2$ NPs. After the surface functionalization of the samples $\gamma Fe_2O_3$ and $CoFe_2O_4$, a pronounced decrease in the remanence ($M_r$) and coercivity ($H_{ci}$) of the samples was noticed because of the increase in the average particle size at the expense of the $SiO_2$-$NH_2$ surface coating. The remanence ($M_r$) thus decreased from 1.17 emu/g for the sample $\gamma Fe_2O_3$ to 0.77 emu/g for the sample $\gamma Fe_2O_3@SiO_2–NH_2$, and from 6.27 emu/g for the sample $CoFe_2O_4$ to 4.43 emu/g for the sample $CoFe_2O_4@SiO_2$-$NH_2$, while the coercivity of the sample $\gamma Fe_2O_3@SiO_2–NH_2$ decreased to 11.32 Oe from 12.55 Oe for the $\gamma Fe_2O_3$, and for the sample $CoFe_2O_4@SiO_2$-$NH_2$ m it decreased to 122.02 Oe from 163.76 Oe for the $CoFe_2O_4$ NPs. The decrease in saturation magnetization ($M_s$), coercivity ($H_{ci}$), and remanent magnetization ($M_r$) in the $\gamma Fe_2O_3@SiO_2–NH_2$ and $CoFe_2O_4@SiO_2–NH_2$ NPs compared to the $\gamma Fe_2O_3$ and $CoFe_2O_4$ NPs was expected due to the larger NP sizes, corresponding to the $SiO_2$ shell and the functionalization with amino (–$NH_2$) groups.

### *2.2. Adsorption and Desorption Tests*

To evaluate the performances and basic adsorption affinity of the $\gamma$-$Fe_2O_3@SiO_2–NH_2$ and $CoFe_2O_4@SiO_2–NH_2$ adsorbents toward $Dy^{3+}$, $Tb^{3+}$, and $Hg^{2+}$ ions in aqueous solutions, batch adsorption experiments at pH 4.5 and with a contact time of 2 h were performed. The graphical representations of the adsorption efficiency and adsorption capacity of the prepared samples are depicted in Figure 8. The numerical results are presented in Table 1.

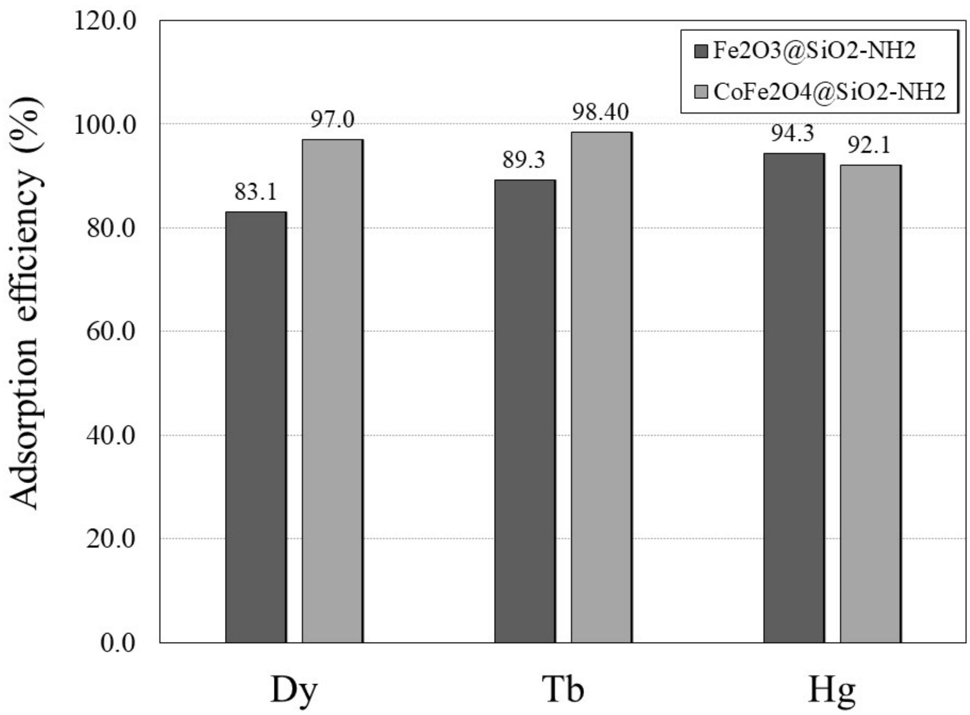


(**a**)

**Figure 8.** *Cont.*

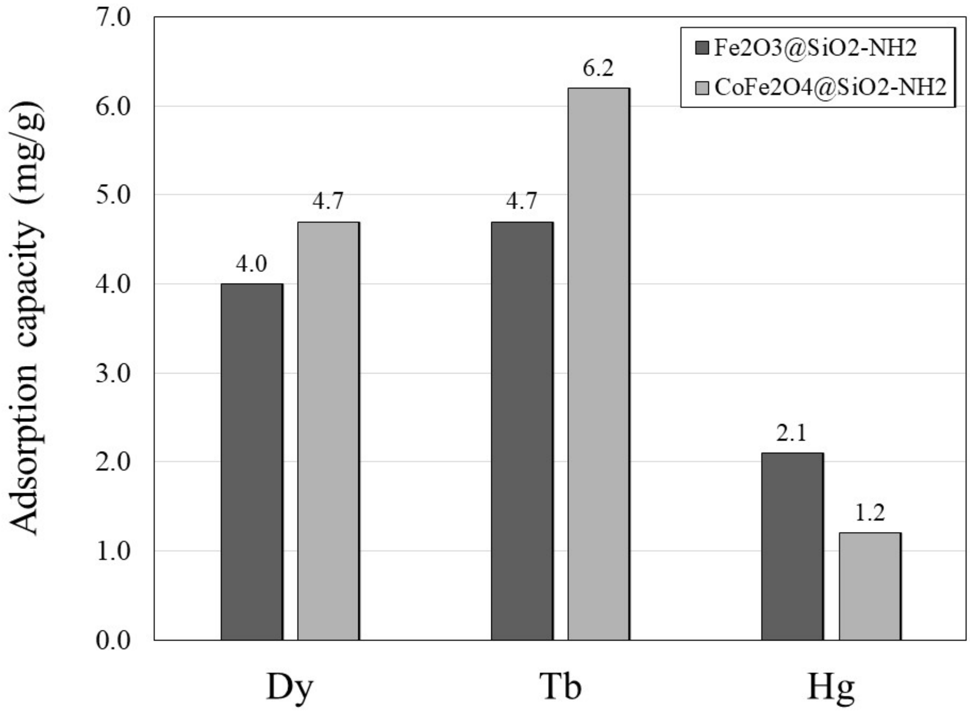


(**b**)

**Figure 8.** (**a**) Adsorption efficiency (%) and (**b**) adsorption capacity (mg/g) of $\gamma Fe_2O_3@SiO_2–NH_2$ and $CoFe_2O_4@SiO_2–NH_2$ NPs toward $Dy^{3+}$, $Tb^{3+}$, and $Hg^{2+}$ ions.

**Table 1.** Results of the adsorption and desorption tests for $Dy^{3+}$, $Tb^{3+}$, and $Hg^{2+}$ ions.

| NPs | Adsorption Efficiency $q_{ads,\%}$ (%) | | | Adsorption Capacity $q_{ads}$ (mg/g) | | | Desorption Efficiency $q_{des}$ (%) | | |
|---|---|---|---|---|---|---|---|---|---|
| | $Dy^{3+}$ | $Tb^{3+}$ | $Hg^{2+}$ | $Dy^{3+}$ | $Tb^{3+}$ | $Hg^{2+}$ | $Dy^{3+}$ | $Tb^{3+}$ | $Hg^{2+}$ |
| $\gamma$-$Fe_2O_3@SiO_2–NH_2$ | 83.1 | 89.3 | 94.3 | 4.0 | 4.7 | 2.1 | 100 | 100 | 100 |
| $CoFe_2O_4@SiO_2–NH_2$ | 97.9 | 98.4 | 92.1 | 4.7 | 6.2 | 1.2 | 100 | 100 | 100 |

The adsorption results of the $Dy^{3+}$, $Tb^{3+}$, and $Hg^{2+}$ ions are presented only for the functionalized NPs, both $\gamma Fe_2O_3@SiO_2–NH_2$ and $CoFe_2O_4@SiO_2–NH_2$, as adsorption by functionalized NPs is usually much more efficient than adsorption by non-functionalized NPs [46].

The adsorption results showed that both the $\gamma Fe_2O_3@SiO_2–NH_2$ and the $CoFe_2O_4@SiO_2–NH_2$ samples had high adsorption affinity towards $Dy^{3+}$ and $Tb^{3+}$ ions, with relatively high adsorption efficiencies of 83.1% and 89.3%, respectively, but low adsorption capacities of 4.0 mg/g and 4.7 mg/g, respectively.

The adsorption affinity of the $\gamma Fe_2O_3@SiO_2–NH_2$ and $CoFe_2O_4@SiO_2–NH_2$ toward the $Dy^{3+}$, $Tb^{3+}$, and $Hg^{2+}$ ions in the aqueous medium can be explained by Pearson's hard-and-soft acid-base (HSAB) theory [91]. This concept is based on Lewis' definition of acids as electron acceptors and bases as electron donors, and it states that soft acids prefer to coordinate and form stronger bonds and more stable complexes with soft bases, whereas hard acids prefer to coordinate and form stronger bonds and more stable complexes with hard bases.

According to the HSAB concept, $Dy^{3+}$ and $Tb^{3+}$ ions are classified as hard Lewis acids, and functional amino ($–NH_2$) groups are classified as hard Lewis bases, so $Dy^{3+}$ and $Tb^{3+}$ ions have a high affinity for $NH_2$ groups. On the other hand, as a soft Lewis acid, $Hg^{2+}$ is a relatively large (1.02 Å) and polarizable atom, which, in practice, prefers to associate with soft bases. Since $Hg^{2+}$ is larger than $Tb^{3+}$ (0.923 Å) and $Dy^{3+}$ (0.912 Å) and, thus, more polarised, it has a weaker preference for interactions with hard $NH_2$ groups. This resulted in its significantly lower adsorption capacity of 2.1 mg/g for the $\gamma Fe_2O_3@SiO_2–NH_2$ and 1.2 mg/g for the $CoFe_2O_4@SiO_2–NH_2$ NPs.

The lower adsorption capacity of $Hg^{2+}$ compared to $Tb^{3+}$ and $Dy^{3+}$, in the context of the HSAB concept, can be explained by the use of the absolute-hardness parameter ($\eta_s$). Parr et al. [92] defined the absolute-hardness parameter as $\eta_s = (I_p - A_s)/2$, where $I_p$ (eV) is the ionization potential and $A_s$ (eV) is the electron affinity. Pearson, in a 1988 paper [93], conveniently provided cumulative experimental values for ionization potential and electron affinity, referring to earlier work by Moore [94]. From these values, it is possible to calculate the absolute-hardness parameter ($\eta_s$) values, which for $Hg^{2+}$, $Tb^{3+}$, and $Dy^{3+}$ are 5.4 eV, 3.1 eV, and 3.1 eV, respectively. Pearson [93] also defined softness ($\sigma_s$) as the inverse of hardness, $\sigma_s = 1/\eta_s$, with zero as the maximum softness. The values of the softness parameter for $Hg^{2+}$, $Tb^{3+}$, and $Dy^{3+}$ are thus 0.19, 0.32, and 0.32, respectively, indicating the softer nature of $Hg^{2+}$ compared to $Tb^{3+}$ and $Dy^{3+}$. Therefore, in this case, a higher complexation affinity of the hard $NH_2$ groups for the hard $Tb^{3+}$ and $Dy^{3+}$ ions and a lower complexation affinity for the softer $Hg^{2+}$ is expected, which also agreed with the results of our work.

A possible explanation for the low adsorption capacity of $Hg^{2+}$ is its unusual chemical properties and its character as a soft Lewis acid. The soft nature of $Hg^{2+}$ is related to its ground-state electronic configuration ($[Xe]4f^{14}5d^{10}6s^2$) with filled electron subshells up to 6s, which, due to its stability, strongly resists electron removal, resulting in the very high ionization potential ($I_p$ 10.434 eV) and moderately high electronegativity ($\chi_P$ 2.00 by Pauling) [95,96] of Hg, which is reflected in its low chemical reactivity [97].

Because all the main energy levels of the Hg atom are filled, and because of the unusually stable $6s^2$ electron pair, Hg can form only very weak hard–soft chemical bonds with amino groups, with a covalent character [96]. Therefore, the interactions of soft Hg with the hard electron-donating N-atom in the $NH_2$ group, which is a small (0.16 Å), low-polarizable atom with high electronegativity ($\chi_P$ 3.04 Pauling) and high ionization potential ($I_p$ 14.534 eV), are not favored [95,98].

In contrast, $Tb^{3+}$ and $Dy^{3+}$, which are hard Lewis acids, according to the HSAB concept, tend to have chemical interactions with the electron-donor N-atoms in the $NH_2$ groups, which have the character of hard Lewis bases. This is due to differences in the stability of their electron configurations and electron-density distributions. Compared to Hg, which has a stable electron configuration, Tb ($[Xe]6s^24f^9$) and Dy ($[Xe]6s^24f^{10}$) have stabilized 4f electrons that do not contribute to the formation of chemical bonds, and their chemical behavior is dictated by the 6 =s valence electrons [97]. Despite the presence of $6s^2$ electrons in addition to the 4f and [Xe] nuclei in Tb and Dy, their most stable oxidation state in aqueous media is +3, which makes them more reactive than divalent Hg. Their chemical reactivity gradually decreases from terbium towards mercury in the sequence of Tb > Dy > Hg [97], which is also reflected in their higher affinity for the formation of complexes with $NH_2$ groups of APTMS compared to Hg. This is consistent with our finding, in this study, that the adsorption capacities of $Tb^{3+}$, $Dy^{3+}$, and $Hg^{2+}$ decrease in the order of $Tb^{3+} > Dy^{3+} > Hg^{2+}$.

On the other hand, the unexpectedly low adsorption capacity of $Tb^{3+}$ and $Dy^{3+}$ ions, which have the character of hard Lewis acids, is probably also due to the strong hydration of these cations in aqueous solutions and the formation of aqua complexes ($[Ln(OH_2)_9]^{3+}$, Ln = Tb, Dy), which is also reflected in their high hydration-enthalpy values for $Tb^{3+}$ ($\Delta H_{hydr}$ −3540 kcal/mol) and $Dy^{3+}$ ($\Delta H_{hydr}$ −3570 kcal/mol) [99–101]. Such aqua complexes are easily formed because of excess water, and they are prone to substitution reactions, in which water molecules are successively replaced by amino ligands and vice versa [102].

Bjerrum [103] determined that a metal complex in an aqueous solution is formed by the exchange of a coordinated water molecule directly bound to the central lanthanide ion ($Ln^{3+}$) with other ligands, provided that the ligand has a sufficiently strong affinity for the lanthanide ion to compete with the affinity of the coordinated water. Such exchanges result in the formation of strong complexes with inner hydration shells [104]. When the ligand replaces the water molecule of the aqua-complex ion, a new metal complex is formed and equilibrium is established. It is assumed that this formation does not take place in one step, but in several steps, involving the following: (i) the joint diffusion of the hydrated cation and anion, (ii) the partial loss of solvent to form the ion pair, (iii) the loss of water from the first coordination sphere of the cation, and (iv) the formation of the complex species. The rate-determining step is the loss of the water molecule from the coordination sphere of the $Ln^{3+}$ ion and, thus, depends only on the hydration properties of the $Ln^{3+}$ ion [105,106].

In general, a maximum number of water molecules are distributed around $Ln^{3+}$ ions during the hydration process, depending on the size of the $Ln^{3+}$ ion and its electronic properties. It is known that the ionic radii of $Ln^{3+}$ ions in the Ln species decrease as the atomic number increases due to lanthanide contraction, which is a consequence of the incomplete mutual protection of the valence f-orbitals.

According to the ratio of the radii of the $Ln^{3+}$ ions to the radii of the oxygen atoms (1.34 Å) in coordinated water molecules ($r_{ion}/r_0$), all the hydrated $Ln^{3+}$-ions in aqueous solutions occupy the configuration of a tricapped trigonal prismatic [107] geometry with six nearly identical water molecules at the vertices of the trigonal prism and the remaining three water molecules capping the prism faces [108].

Hydrates of the lighter $Ln^{3+}$ ions ($La^{3+}$-$Nd^{3+}$) have a regular tricapped trigonal prismatic configuration, with slightly longer bond distances from the $Ln^{3+}$ ion to the capping water molecules (Ln-O) than to the water molecules forming the prism. The decrease in the radii of the $Ln^{3+}$-ions with the increase in the atomic number of the Ln-species starting from $Nd^{3+}$ does not, in principle, affect the structure of the prism, but has a strong effect on the more weakly bound capping positions of the water molecules in the prismatic structure, resulting in a partial loss of the water molecules in the capping positions for the heaviest $Ln^{3+}$-ions ($Ho^{3+}$-$Lu^{3+}$). In fact, studies have shown that the bond strength of the three-capping water molecules is strong at the beginning of the Ln series for nonahydrates (e.g., $La^{3+}$-$Sm^{3+}$), while in the Ln series starting from ($Sm^{3+}$-$Lu^{3+}$), the Ln–O capping bonds become weaker and shorter at the same time. The Ln–O change in the $[Ln(OH_2)_9]^{3+}$ for $Ln^{3+}$-ions (e.g., $La^{3+}$, $Sm^{3+}$, $Tb^{3+}$, $Dy^{3+}$, $Ho^{3+}$, and $Lu^{3+}$) occurs in the following sequence: La-O (2.52 Å) > Sm-O (2.46 Å) > Tb-O (2.39 Å) > Dy–O (2.37 Å) > Ho–O (2.36 Å) > Lu–O (2.31 Å) [109]. Consequently, in the lanthanide series starting from $Sm^{3+}$ onward, the three water molecules in the structure are not equally strongly bound and one of the water molecules is at a shorter distance from the Ln-center than the other two. In the series from $Ho^{3+}$ to $Lu^{3+}$, the water deficit and the differences between the strongly bound water molecules and the more weakly-bound molecules are even greater [108,109].

Therefore, since Ln-O bonds are more easily broken, in the whole Ln series, the lighter lanthanide $Ln^{3+}$ -ions ($La^{3+}$–$Nd^{3+}$) form stable nonahydrates, while the heavier $Ln^{3+}$-ions ($Ho^{3+}$–$Lu^{3+}$) form octahydrates. Intermediate $Ln^{3+}$-ions ($Sm^{3+}$–$Dy^{3+}$) favor the formation of complex forms of nona- and octahydrates with non-integer coordination numbers (CN) between 8 and 9. Therefore, the CN of these intermediate lanthanides should be average with respect to the ratio of nona- to octahydrate forms [110,111].

Such Ln-O bond behavior determines the hydration behavior of $Ln^{3+}$ ions and explains their very unusual and complex ligand exchange kinetics throughout the Ln series [110,111]. The peculiarity is that the exchange rate of water molecules between the first hydration shell and the bulk solvent increases in the direction from $La^{3+}$ to $Gd^{3+}$, reaches its maximum in the central region of the Ln series ($Tb^{3+}$, $Dy^{3+}$), and then decreases up to $Lu^{3+}$ [112,113]. The physical reasons for these phenomena are still not well understood and are the subject of many investigations [110,111].

On the other hand, $H_2O$ is also known to be a hard base [114], which, in accordance with the HSAB concept and the above values of absolute hardness, associates with hard ligands rather than soft ligands, because, in this case, hard–hard interactions are more favorable. Since the amino ($–NH_2$) group is a hard Lewis base, the substitution of the amino ligand and $H_2O$ is relatively favorable from this point of view [100,114], which makes lanthanide-ion complexes of $Ln^{3+}$ (Ln = Tb, Dy) extremely labile [115]. In contrast, for transition metals, the lability of complexes generally varies with their electronic configuration. Some complexes are labile, while others are kinetically very inert, such as $d^3$ species and low-spin $d^6$ species, with high stabilities and high activation energies for ligand substitution [115].

The formation of amino complexes is largely related to the availability of active sites on the adsorbent surfaces and the coordination number. The two key factors influencing the coordination number and complex formation, as well as their chemical stability, areas follows: (i) the influence of the donor N-atoms in the immediate vicinity of the metal ion ($Tb^{3+}$, $Dy^{3+}$, $Hg^{2+}$), which, due to interatomic tension, prevent more N-atoms from making contact with the metal ion; and (ii) the steric repulsions between the larger substituent groups in the APTMS, which are bonded to the donor N-atom (i.e., $H_2N(CH_2)_3$-), which determine how much of the ligand can be surrounded by the metal ion [115]. The lack of available active sites thus reduces the ability to form complexes, resulting in a lower adsorption capacity.

The electron-donating N-atoms of the amino groups of APTMS in the surface coating of the adsorbent possess a free-electron pair that can be donated to form a coordination bond with the $Tb^{3+}$, $Dy^{3+}$, and $Hg^{2+}$ metal ions in the aqueous medium. Depending on the coordination number, which is 9 for $Tb^{3+}$ and $Dy^{3+}$ [98,116] and 6 for $Hg^{2+}$ [117,118], these metal ions can coordinate linearly with one or two amino groups, with the remaining coordination sites occupied by water molecules. Thus, the coordination mechanism of $Tb^{3+}$, $Dy^{3+}$, and $Hg^{2+}$ with the amino groups of APTMS on the surfaces of $\gamma Fe_2O_3@SiO_2–NH_2$ and $CoFe_2O_4@SiO_2–NH_2$ adsorbents can be represented as [101,119,120]:

$$RNH_2 + Ln^{3+} \Leftrightarrow [Ln(RNH_2)(H_2O)_8]^{3+} \text{ (Ln = Tb, Dy)} \quad (1)$$

$$RNH_2 + Hg^{2+} \Leftrightarrow [Hg(RNH_2)(H_2O)_5]^{2+} \quad (2)$$

After the adsorption of $Tb^{3+}$, $Dy^{3+}$, and $Hg^{2+}$, the possibility of recovering both adsorbents, $\gamma Fe_2O_3@SiO_2–NH_2$ and $CoFe_2O_4@SiO_2–NH_2$, for the reuse and recycling of $Tb^{3+}$, $Dy^{3+}$, and $Hg^{2+}$ ions were verified by a desorption process. The choice of agent for desorption is based on the type of adsorbate–adsorbent system [121] and depends mainly on the compatibility between adsorbate and adsorbent, the pH and ionic strength of the medium, the complexation ability, the desorption-agent content, and the exposure time, as these variables can modify the desorption behavior or destroy the adsorbent structure [121]. In addition, desorption phenomena are related to a series of surface interactions and diffusion into micropores or the intraparticle spaces of the adsorbents [99].

In our previous research [122,123], we studied some desorption conditions and the use of different acidic desorption agents, such as hydrochloric acid (HCl), nitric acid ($HNO_3$), and citric acid, and we found that $HNO_3$ gave better results than the other two desorption agents. Therefore, in the present study, a desorption procedure for $Tb^{3+}$, $Dy^{3+}$, and $Hg^{2+}$ was carried out using a 1-M aqueous solution of $HNO_3$ for 1 h at room temperature and with pH 4.5 [124]. The desorption was carried out in one cycle only due to the loss of material during the desorption process. The results of the desorption efficiency are shown graphically in Figure 9. After 1 h, the $Tb^{3+}$, $Dy^{3+}$, and $Hg^{2+}$ ions were completely desorbed from the surfaces of the $\gamma Fe_2O_3@SiO_2–NH_2$ and $CoFe_2O_4@SiO_2–NH_2$ adsorbents, indicating the potential for the stable reusability of the prepared adsorbents and the high potential of these adsorbents for the recycling and removal of heavy metals.

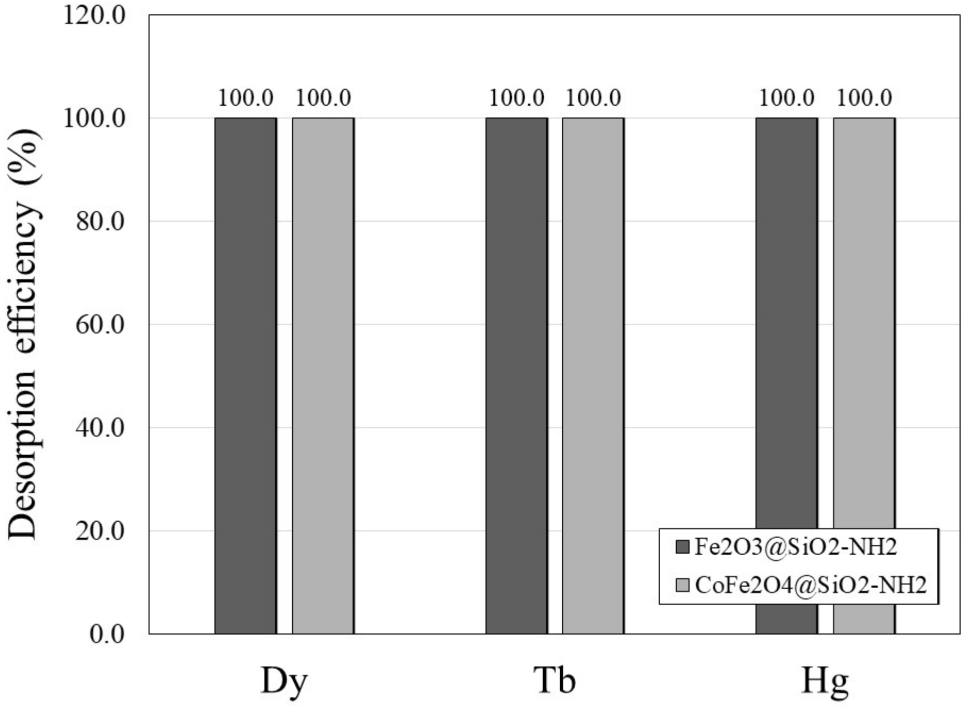


**Figure 9.** Desorption efficiency of $\gamma Fe_2O_3@SiO_2–NH_2$ and $CoFe_2O_4@SiO_2–NH_2$ NPs.

Table 2 shows the comparison of the adsorption of the $Dy^{3+}$, $Tb^{3+}$, and $Hg^{2+}$ ions onto the prepared $\gamma Fe_2O_3@SiO_2–NH_2$ and $CoFe_2O_4@SiO_2–NH_2$ NPs with the adsorption of $Dy^{3+}$, $Tb^{3+}$, and $Hg^{2+}$ on different adsorbents. It can be observed that the adsorption conditions, such as the initial adsorbate concentration ($c_{ads,0}$), adsorbent dosage ($\gamma_{ads}$), time of adsorption ($t_{ads}$), adsorption temperature ($T_{ads}$), and solution pH, were very different, making the comparison of the adsorption performances a difficult and a complex task.

**Table 2.** The adsorption capacity of $Dy^{3+}$, $Tb^{3+}$, and $Hg^{2+}$ with various adsorbent materials.

| Adsorbent (NPs) | Adsorbate | Adsorption Conditions | | | | | Adsorption/Desorption Characteristics | | | Ref. |
|---|---|---|---|---|---|---|---|---|---|---|
| | | $c_{ads,0}$ (mg/L) | $\gamma_{ads,NPs}$ (g/L) | $t_{ads}$ (min) | $T_{ads}$ (°C) | pH | $q_{ads}$ (mg/g) | $q_{ads,\%}$ (%) | $q_{des,\%}$ (%) | |
| | **Dysprosium ($Dy^{3+}$)** | | | | | | | | | |
| $Fe_3O_4@SiO_2$@polyaniline–graphene oxide | $Dy^{3+}$ | 0.01 | 0.4 | 2 | 25 | 4 | 16.0 | 98 | 95 | [125] |
| $Fe_3O_4–C_{18}$–chitosan–DETA | $Dy^{3+}$ | 50 | 1.0 | 720 | 25 | 7 | 28.3 | >80 | >95 | [126] |
| $\gamma$-$Fe_2O_3$-$NH_4OH@SiO_2$ (APTMS) | $Dy^{3+}$ | 8.125 | 3.0 | 120 | 25 | 7 | 23.2 | 94 | N/A | [84] |
| Synthetic-polymer-based magnetic adsorbent (M-PPTA) | $Dy^{3+}$ | 50 | 3.0 | 130 | 25 | 5.5 | 24.0 | 98.4 | >84 | [127] |
| Polymeric adsorbents modified with ethylenediamine (EDA) and diglycolamic acid (DGA) | $Dy^{3+}$ | 162.5 | 10.0 | 4320 | 25 | 1 | 18.4 | 30 | N/A | [128] |
| Chemically activated carbons from spent-coffee waste | $Dy^{3+}$ | 5.0 | 0.3 | 120 | 25 | 4 | 31.26 | 96 | N/A | [129] |
| Physically activated carbons from spent-coffee waste | | | | | | | 33.52 | 99 | | |
| *Ulva lactuca*—Chlorophyta (green) | $Dy^{3+}$ | 0.5 | 3.0 | 4320 | 25 | N/A (1) | 0.570 | 89 | N/A | [130] |
| *Gracilaria* sp.—Rhodophyta (red) | | | | | | | 0.526 | 84 | | |
| $Fe^0–SiO_2$–PA/$SiO_2$–DTPA | $Dy^{3+}$ | 1.5 | 0.5 | 30 | 21 | 3 | 1.85 | N/A | N/A | [131] |
| $\gamma Fe_2O_3@SiO_2–NH_2$ | $Dy^{3+}$ | 32 | 2.5 | 120 | 25 | 4 | 4.0 | 83.1 | 100 | This work |

**Table 2.** *Cont.*

| Adsorbent (NPs) | Adsorbate | Adsorption Conditions | | | | | Adsorption/Desorption Characteristics | | | Ref. |
|---|---|---|---|---|---|---|---|---|---|---|
| | | $c_{ads,0}$ (mg/L) | $\gamma_{ads,NPs}$ (g/L) | $t_{ads}$ (min) | $T_{ads}$ (°C) | pH | $q_{ads}$ (mg/g) | $q_{ads,\%}$ (%) | $q_{des,\%}$ (%) | |
| $CoFe_2O_4$@$SiO_2$–$NH_2$ | $Dy^{3+}$ | 32 | 2.5 | 120 | 25 | 4 | 4.7 | 97.9 | 100 | This work |
| | **Terbium ($Tb^{3+}$)** | | | | | | | | | |
| $Fe_3O_4$@$SiO_2$@polyaniline-graphene oxide | $Tb^{3+}$ | 0.01 | 0.4 | 2 | 25 | 4 | 11.8 | 98 | 95 | [125] |
| $Fe^0$–$SiO_2$–PA/$SiO_2$–DTPA | $Tb^{3+}$ | 1.5 | 0.5 | 30 | 21 | 3 | 1.4 | N/A | N/A | [131] |
| Molecular-sieve zeolite<br>*B. cereus* biomass-supported zeolite | $Tb^{3+}$ | 20 | 0.5 | 2880 | 25 | 5 | 2.59<br>5.07 | 80 | >60 | [132] |
| Multi-walled carbon nanotubes with tannic acid (TA-MWCNTs) | $Tb^{3+}$ | 40 | 5 | 60 | 20 | 5 | 8.55 | N/A | >95 | [133] |
| γ-$Fe_2O_3$–$NH_4OH$@$SiO_2$ (APTMS) | $Tb^{3+}$ | 0.32 | 1.5 | 120 | 25 | 7 | 0.204 | 93 | N/A | [134] |
| γ$Fe_2O_3$@$SiO_2$–$NH_2$ | $Tb^{3+}$ | 32 | 2.5 | 120 | 25 | 4 | 4.7 | 89.3 | 100 | This work |
| $CoFe_2O_4$@$SiO_2$–$NH_2$ | $Tb^{3+}$ | 32 | 2.5 | 120 | 25 | 4 | 6.2 | 98.4 | 100 | This work |
| | **Mercury ($Hg^{2+}$)** | | | | | | | | | |
| $CoFe_2O_4$–chitosan–graphene | $Hg^{2+}$ | 20 | 0.12 | 230 | 50 | 7 | 361.0 | 90 | <5 | [135] |
| Polypyrrole-functionalized magnetic Kaolin (Ppy-$Fe_3O_4$/kaolin) | $Hg^{2+}$ | 50 | 0.05 | 420 | 42 | 7.2 | 317.1 | N/A | >90 | [136] |
| $CoFe_2O_4$@$SiO_2$–$NH_2$ | $Hg^{2+}$ | 20 | 0.1 | 720 | 25 | 7 | 149.3 | N/A | 75 | [137] |
| $CoFe_2O_4$@$SiO_2$–EDTA | $Hg^{2+}$ | 20 | 0.1 | 720 | 25 | 7 | 103.3 | >90 | >90 | [138] |
| γ-$Fe_2O_3$@$NH_2$ | $Hg^{2+}$ | 200 | 2.25 | 30 | 25 | 7 | 85.6 | 84 | 100 | [122] |
| $Fe_3O_4$<br>$Fe_3O_4$–$Ag^0$ | $Hg^{2+}$ | 100 | 2.5 | 720 | 23 | N/A (2) | 28.0<br>71.3 | <40<br>>80 | N/A | [139] |
| Rice-husk-activated carbon (RHAC) | $Hg^{2+}$ | 20 | 0.2 | 60 | 25 | 5 | 55.87 | N/A | N/A | [140] |
| Magnetic poly(vinyl alcohol)—procion blue MX-3G<br>Magnetic poly(vinyl alcohol) (mPVAL) | $Hg^{2+}$ | 400 | 5.0 | 10 | 20 | 6 | 69.2<br>0.57 | >94 | 95 | [141] |
| Amino-functionalized $SiO_2$ particles ($NH_2$@$SiO_2$) | $Hg^{2+}$ | 100 | 2.25 | 60 | 25 | 4 | 3.75 | 88 | 100 | [123] |
| Activated carbon<br>Gold-NP-coated silica | $Hg^{2+}$ | 0.1–300 | 2.3 | 1440 | 22 | 7.4 | 2.5<br>1.4 | 95<br>96 | N/A | [142] |
| γ$Fe_2O_3$@$SiO_2$–$NH_2$ | $Hg^{2+}$ | 40 | 2.5 | 120 | 25 | 4 | 2.1 | 94.3 | 100 | This work |
| $CoFe_2O_4$@$SiO_2$–$NH_2$ | $Hg^{2+}$ | 40 | 2.5 | 120 | 25 | 4 | 1.2 | 92.1 | 100 | This work |

(1) Seawater (salinity 0.175 mol/L–0.525 mol/L); (2) pH not adjusted.

Su et al. [125] studied the adsorption capacity of $Dy^{3+}$ with the adsorbate $Fe_3O_4$@$SiO_2$@polyaniline-graphene oxide, and they demonstrated an adsorption capacity of 16.0 mg/g, an adsorption efficiency of 98%, and a desorption efficiency of 95% at pH 4. Liu et al. [126] reported an adsorption capacity of 28.3 mg/g, an adsorption efficiency of >80%, and a desorption efficiency of >95% for $Dy^{3+}$ at pH 7 using $Fe_3O_4$-$C_{18}$–chitosan–DETA. With the same pH of 7, using $NH_4OH$@$SiO_2$ (APTMS), Kegl et al. [84] reported an adsorption capacity of 23.2 mg/g and an adsorption efficiency of 94% for $Dy^{3+}$. Javadian et al. [127] reported the adsorption characteristics of synthetic-polymer-based magnetic adsorbent (M-PPTA) toward $Dy^{3+}$ at pH 5.5, and found an adsorption capacity of 24.0 mg/g, an adsorption efficiency of 98.4%, and a desorption efficiency of >84%. Shinozaki et al. [128] noted 18.4 mg/g of adsorption capacity and 30% of adsorption efficiency for $Dy^{3+}$ at pH 1 using an adsorbate of polymeric adsorbents modified with ethylenediamine (EDA) and diglycolamic acid (DGA).

Alcaraz et al. [129] reported the use of chemically and physically activated carbons from spent-coffee waste to adsorbed $Dy^{3+}$ ions. They showed an adsorption capacity of chemically activated carbons toward $Dy^{3+}$ of 31.26 mg/g and an adsorption efficiency of $Dy^{3+}$ of 96% at pH 4. When using physically activated carbons from spent-coffee waste, an adsorption capacity of 33.52 mg/g and an adsorption efficiency of 99% were obtained. Further, Viana et al. [130] reported an adsorption capacity of 0.570 mg/g and an adsorption efficiency of 89% for $Dy^{3+}$ using *ulva lactuca*—Chlorophyta (green), while an adsorption capacity of 0.526 mg/g and an adsorption efficiency of 84% were obtained for $Dy^{3+}$ by using *Gracilaria* sp.—Rhodophyta (red). According to Zhang et al. [131], an adsorption capacity of 1.85 mg/g and an adsorption efficiency of 84% of $Dy^{3+}$ at pH 3 were obtained using an $Fe^0$–$SiO_2$–PA/$SiO_2$–DTPA adsorbent.

Su et al. [125], Zhang et al. [131], Barros et al. [132], Tong et al. [133], and Kegl et al. [134] studied the adsorption capacity of $Tb^{3+}$ using various adsorbent materials under different adsorption conditions. Using graphene oxide at pH 4, Su et al. [125] obtained an adsorption capacity of 11.8 mg/g, an adsorption efficiency of 98%, and a desorption efficiency of 95% for $Tb^{3+}$. Zhang et al. [131] used an $Fe^0$–$SiO_2$–PA/$SiO_2$–DTPA adsorbate at a pH of 3 and obtained an adsorption capacity of 1.4 mg/g for $Tb^{3+}$. Barros et al. [132] reported the use of molecular-sieve zeolite for the adsorption of $Tb^{3+}$ ions at a pH of 5, and they noted an adsorption capacity of 2.59 mg/g alongside an adsorption efficiency of 80%, and a desorption efficiency of >60% for $Tb^{3+}$; furthermore, they obtained an adsorption capacity of 5.07 mg/g for the $Tb^{3+}$ using *B. cereus* biomass-supported zeolite adsorbate. Tong et al. [133] used multi-walled carbon nanotubes with tannic acid (TA-MWCNTs) for the adsorption of $Tb^{3+}$ at pH 5 and obtained an adsorption capacity of 8.55 mg/g, while Kegl et al. [134] used a superparamagnetic $\gamma$-$Fe_2O_3$-$NH_4OH$@$SiO_2$ (APTMS) adsorbent and obtained an adsorption capacity of 0.204 mg/g for the adsorption of $Tb^{3+}$ ions from water at a pH of 7.

Adsorption studies on $Hg^{2+}$ ions with $CoFe_2O_4$–chitosan–graphene, polypyrrole-functionalized magnetic kaolin (Ppy-$Fe_3O_4$/kaolin), and $CoFe_2O_4$@$SiO_2$–$NH_2$ adsorbents at a pH of 7 showed adsorption capacities of 361.0 mg/g, 255.2 mg/g, and 149.3 mg/g, respectively. These studies were performed by Zhang et al. [135], Lin et al. [136], and Wang et al. [137], respectively.

In recent works, Xia et al. [138], Allwin Mabes Raj et al. [122], and Inglezakis et al. [139] studied the adsorption of $Hg^{2+}$ using $CoFe_2O_4$@$SiO_2$–EDTA, $\gamma$–$Fe_2O_3$@$NH_2$, and $Fe_3O_4$ as adsorbates, and they noted adsorption capacities of 103.3 mg/g, 85.6 mg/g, and 28.0 mg/g for $Hg^{2+}$, respectively. Liu et al. [140] studied the adsorption capacity of $Hg^{2+}$ with the adsorbate rice-husk-activated carbon (RHAC) and demonstrated an adsorption capacity of 55.87 mg/g at a pH of 5. Denizli et al. [141] studied the adsorption of $Hg^{2+}$ with magnetic poly (vinyl alcohol)—procion blue MX-3G as the adsorbent and noted an adsorption capacity of 69.2 mg/g, an adsorption efficiency of >94%, and a desorption capacity of 95% for $Hg^{2+}$. An adsorption study of $Hg^{2+}$ with amino-functionalized $SiO_2$ particles ($NH_2$@$SiO_2$) conducted by Raj et al. [123] and a study with activated carbon performed by Solis et al. [142] showed adsorption capacities of 3.75 mg/g and 2.5 mg/g, respectively.

Nevertheless, it can be observed that the adsorption of $Dy^{3+}$, $Tb^{3+}$, and $Hg^{2+}$ ions is tested mostly in acidic or neutral aqueous media, and that the adsorption capacity is higher in surface-functionalized adsorbent nanomaterials. In addition, some adsorbents have significantly higher adsorption properties for $Hg^{2+}$ than for $Dy^{3+}$ and $Tb^{3+}$ ions compared to our prepared adsorbent materials. However, the main advantages of our adsorbents are their relatively fast kinetics of adsorption, which are associated with their nano-size and functionality, their high desorption efficiency, and the convenient and highly efficient sustainable recovery of the used adsorbate material at the end of the adsorption process by magnetic attraction.

### 2.3. Cytotoxicity Study

The cytotoxicity of the nanoparticles was tested in different healthy cell lines after 3 days of incubation. In the SKMDCs, the $\gamma Fe_2O_3$ nanoparticles showed lower toxicity than the $\gamma Fe_2O_3@SiO_2–NH_2$, as shown in Figure 10a. The cell viability reached 69 ± 0.72% after 3 days of incubation with 5 µg/mL of $\gamma Fe_2O_3@SiO_2–NH_2$, which decreased to 57 ± 0.47% at a concentration of 500 µg/mL. Similarly, the $CoFe_2O_4$ nanoparticles showed lower toxicity than the $CoFe_2O_4@SiO_2–NH_2$. The incubation of the SKMDCs with $CoFe_2O_4@SiO_2–NH_2$ up to a concentration of 125 µg/mL for 3 days showed lower toxicity with a cell viability above 80%; however, the cell viability decreased to 70 ± 3.41% at 500 µg/mL.

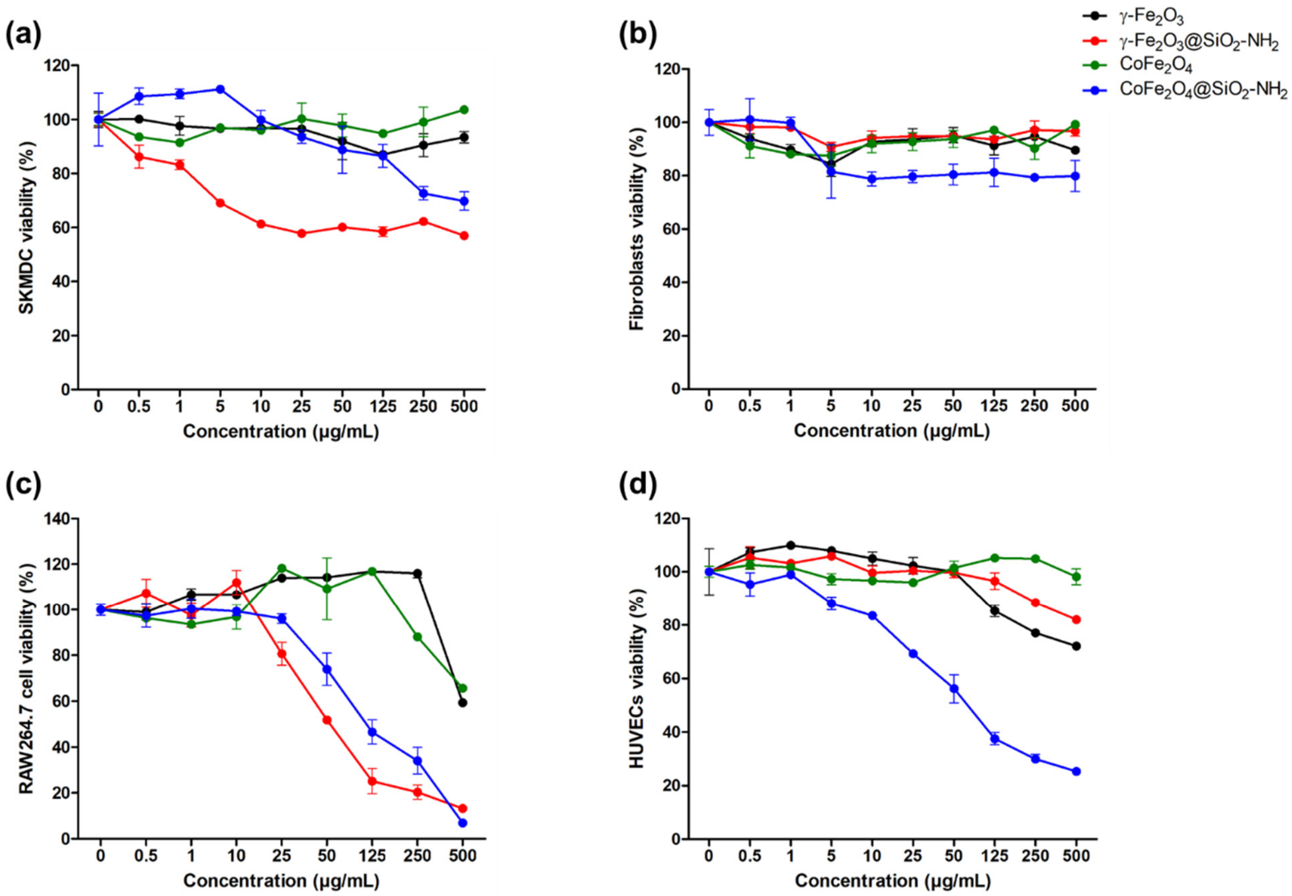


**Figure 10.** Cell viability (%) of (**a**) SKMDCs, (**b**) fibroblasts, (**c**) RAW264.7, and (**d**) HUVECs treated with different concentrations of nanoparticles for 3 days. Results are presented as mean ± SEM, n = 3.

In the fibroblasts, all the nanoparticles showed lower toxicity when the cell viability was above 80%, with concentrations of up to 500 µg/mL (Figure 10b).

In the macrophage RAW264.7 cell line, both the $\gamma Fe_2O_3$ and the $CoFe_2O_4$ showed lower toxicity than the $\gamma Fe_2O_3@SiO_2–NH_2$ and $CoFe_2O_4@SiO_2–NH_2$ (Figure 10c). At 50 µg/mL, the cell viability reached 52 ± 0.61% and 74 ± 7% for the $\gamma Fe_2O_3@SiO_2–NH_2$ and $CoFe_2O_4@SiO_2–NH_2$, respectively. However, at 500 µg/mL, the cell-viability values were 59 ± 0.10%, 13 ± 0.51%, 66 ± 0.31%, and 7 ± 0.23% for the $\gamma Fe_2O_3$, $\gamma Fe_2O_3@SiO_2–NH_2$, $CoFe_2O_4$, and $CoFe_2O_4@SiO_2–NH_2$, respectively. It is worth mentioning that the macrophage RAW264.7 cells were more sensitive to the $\gamma Fe_2O_3@SiO_2–NH_2$ and $CoFe_2O_4@SiO_2–NH_2$ than the other cell lines.

The toxicity of the nanoparticles was also tested in the HUVECs (Figure 10d). The results showed the low toxicity of the $\gamma Fe_2O_3$, $\gamma Fe_2O_3@SiO_2–NH_2$, and $CoFe_2O_4$ compared with the $CoFe_2O_4@SiO_2–NH_2$, which showed a decrease in cell viability (69 ± 1.26%) at 25 µg/mL, reaching 25 ± 0.86% at 500 µg/mL.

The results presented in Figure 11a show that none of the nanoparticles had hemolytic effects, except the nanoparticles of $\gamma Fe_2O_3@SiO_2{-}NH_2$, which showed a dose-dependent hemolytic effect. A change in the supernatant color was observed by the naked eye at concentrations of 50 μg/mL and above, indicating the lysis of red blood cells and hemoglobin release (Figure 11b) [5].

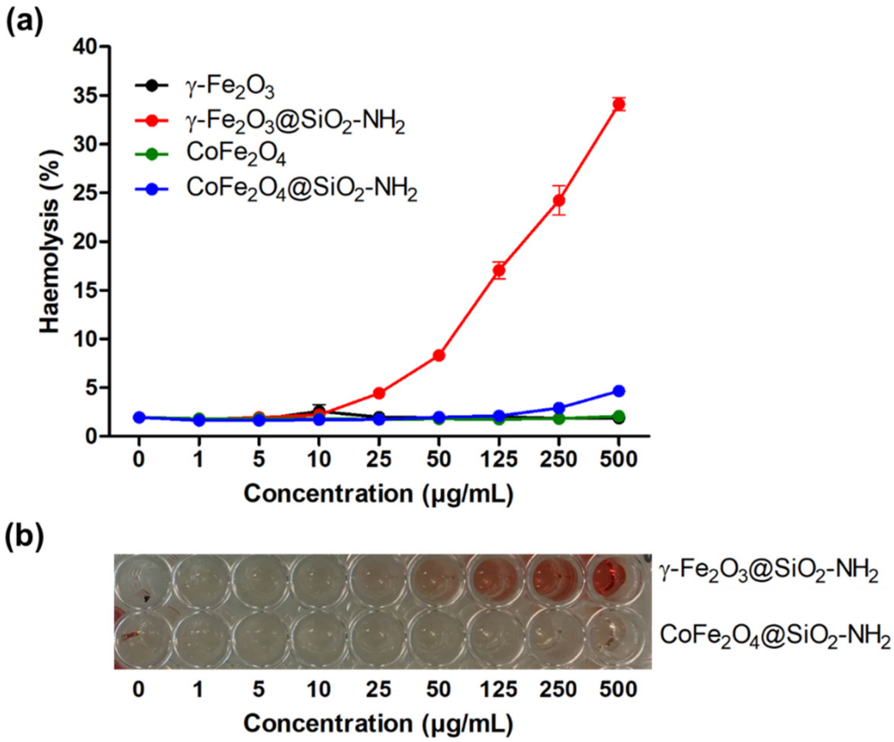


**Figure 11.** In vitro hemolytic studies. (**a**) Hemolytic effect of different nanoparticles on human blood at different concentrations (**a**), representative image of the hemolytic effect (red-colored supernatant) of nanoparticles (**b**).

A toxicity study on zebrafish embryos exposed to different concentrations of nanoparticles as shown in Figure S3 revealed that none of the nanoparticles had toxic effects on the zebrafish embryos until 96 hpf compared to the control, even at a high concentration of 500 mg/L (Figure 12).

Table S1 depicts the list of various adsorbent materials with their toxicological assessment in different biological systems. Many studies investigating the toxicities of different materials using in vivo and in vitro studies, such as a toxicity study of human kidneys (HEK293) using magnetic, $SiO_2$-coated nanoparticles with an exposure of up to 1.0 μg/μL for 12 h, which was reported by Shim et al. [143]. In their $SiO_2$ in vitro study, Pisani et al. [144] used A549 (human) lung cells with 0.1–6-μg/cm$^2$ dosages and exposed them for 24 h. A toxicity study was reported by Ellinger-Ziegelbauer and Pauluhn [145] on rat-lung cells with MWCNT at a 11-mg/m$^3$ concentration for a 6-h (aerosol) 90-day post-exposure period. Jovanović et al. [146] studied the $TiO_2$ (anatase) and hydroxylated fullerene toxicity of 40-μg/mL fullerenes and 170 ng/mL in Danio rerio (embryo). With 2.5 μg/mL and 25 μg/mL of Ag in human colon cells, toxicity was studied by Böhmert et al. [147]. Conde et al. [148] studied toxicity using Au, functionalized with anti-sense cDNAs at dosages of 30 nM in the HCT-116 (human) colon.

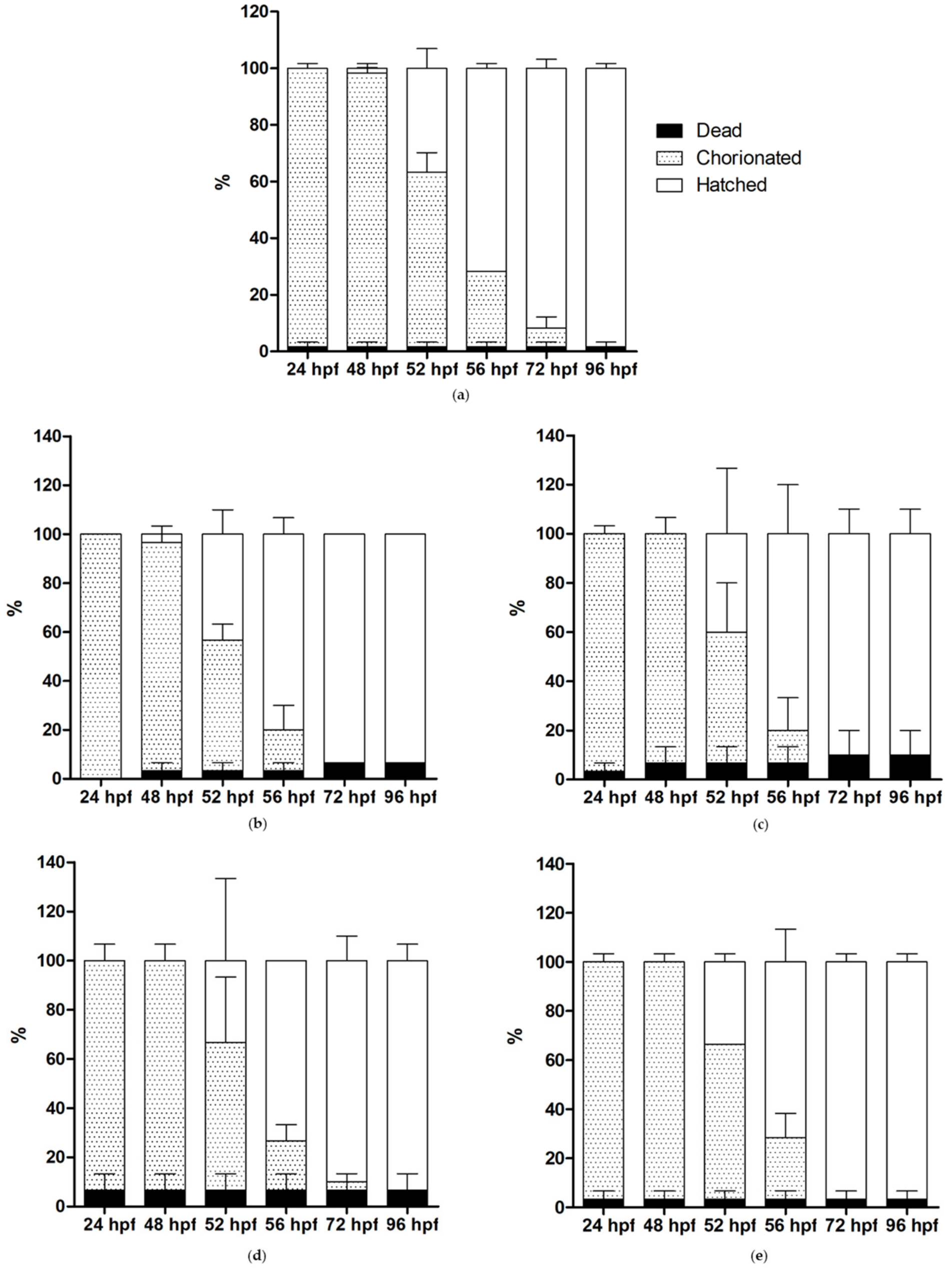


**Figure 12.** Zebrafish-embryo development expressed as percentages of dead, chorionated, and hatched, in water containing concentration of 500 mg/L of nanoparticles. Control group (**a**) is of growth without the use of any NPs (**b**) $\gamma Fe_2O_3$ (**c**) $\gamma Fe_2O_3@SiO_2–NH_2$ (**d**) $CoFe_2O_4$, and (**e**) $CoFe_2O_4@SiO_2–NH_2$ for 24, 48, 52, 56, 72, and 96 h post-fertilization (hpf). Data are presented as mean ± SEM of two independent experiments.

Our present study investigating the cytotoxicity of iron-oxide NPs generally showed that both these NPs, $\gamma Fe_2O_3@SiO_2–NH_2$ and $CoFe_2O_4@SiO_2–NH_2$, are non-toxic.

## 3. Materials and Methods

All the chemicals used in this study were generally of reagent grade, obtained from commercial sources without further purification: iron (II) chloride tetrahydrate ($FeCl_2 \cdot 4H_2O$, 98%, 198.81 g/mol, CAS no. 13478-10-9, Sigma-Aldrich, Merck Group KGaA, Darmstadt, Germany), iron (III) chloride hexahydrate ($FeCl_3 \cdot 6H_2O$, ≥98%, 270.3 g/mol, CAS no. 10025-77-1, Sigma-Aldrich, Merck Group KGaA, Darmstadt, Germany), cobalt (II) chloride hexahydrate ($CoCl_2 \cdot 6H_2O$, 98%, 237.93 g/mol, CAS no. 7791-13-1, Sigma-

Aldrich, Merck Group KGaA, Darmstadt, Germany), ammonium hydroxide aqueous solution ($NH_4OH$, 25%, 35.05 g/mol, 0.91 g/mL, CAS no. 1336-21-6, GramMol, Zagreb, Croatia), sodium hydroxide (NaOH, ≥98% (anhydrous), 40 g/mol, CAS no. 1310-73-2, Sigma-Aldrich, Merck Group KGaA, Darmstadt, Germany), potassium hydroxide (KOH, 1 mol/L (1-N), Titripur®, 56.11 g/mol, 1.05 g/mL, CAS no. 1310-58-3, Sigma-Aldrich, Merck Group KgaA, Darmstadt, Germany), potassium chloride (KCl, ACS reagent, 99.0–100.5%, 74.55 g/mol, CAS no. 7447-40-7, Sigma-Aldrich, Merck Group KgaA, Darmstadt, Germany), hydrochloric acid (HCl, for 1000 mL, 1 mol/L (1-N), Titrisol®, 36.46 g/mol, 1.09 g/ml, CAS no. 7647-01-0, Sigma-Aldrich, Merck Group KgaA, Darmstadt, Germany), nitric acid ($HNO_3$, ACS reagent, 70%, 63.01 g/mol, 1.413 g/mL, CAS no. 7697-37-2, Sigma-Aldrich, Merck Group KgaA, Darmstadt, Germany), 2-propanol ($C_3H_8O$, 99.8%, 60.1 g/mol, 0.785 g/mL, CAS no. 67-63-0, GramMol, Zagreb, Croatia), ethanol ($C_2H_5OH$, 96%, 46.07 g/mol, 0.810 g/mL, CAS no. 64-17-5, GramMol, Zagreb, Croatia), tetraethyl orthosilicate TEOS ($C_6H_{20}O_4Si$, 99%, 208.33 g/mol, 0.94 g/mL, CAS no. 78-10-4, Sigma-Aldrich, Merck Group KGaA, Darmstadt, Germany), 3-aminopropyltrimethoxysilane APTMS ($C_6H_{17}NO_3Si$, 97%, 179.29 g/mol, 1.027 g/mL, CAS no. 13822-56-5, Sigma-Aldrich, Merck Group KGaA, Darmstadt, Germany), terbium (III) chloride hexahydrate ($TbCl_3{\cdot}6H_2O$, 99.9%, 373.38 g/mol, CAS no. 13798-24-8, Sigma-Aldrich, Merck Group KGaA, Darmstadt, Germany), dysprosium (III) nitrate pentahydrate ($Dy(NO_3)_3{\cdot}5H_2O$, 99.9%, 438.59 g/mol, CAS no. 10031-49-9, Sigma-Aldrich, Merck Group KGaA, Darmstadt, Germany), and mercury (II) nitrate monohydrate ($Hg(NO_3)_2{\cdot}H_2O$, ≥98.5%, 342.62 g/mol, CAS no. 7783-34-8, Sigma-Aldrich, Merck Group KGaA, Darmstadt, Germany). For the preparation of all suspensions and solutions, deionized water ($dH_2O$) was used.

### *3.1. Synthesis of Magnetic Nanoparticles (MNPs)*

Spinel-type MNPs of maghemite ($\gamma$-$Fe_2O_3$) and Co-ferrite ($CoFe_2O_4$) were obtained by co-precipitation of $M^{2+}$ (M = Fe, Co) and $Fe^{3+}$ salts at slightly elevated temperature in an alkaline aqueous medium according to Schikorr reaction [149]:

$$M^{2+} + 2Fe^{3+} + 4OH^{-} + O_2 = MO{\cdot}Fe_2O_{3\,(s)}\downarrow + 2H_2O \quad (3)$$

#### 3.1.1. $\gamma$-$Fe_2O_3$ NPs

For the synthesis of $\gamma Fe_2O_3$ NPs, 50 mL of 25% $NH_4OH$ in a round-bottomed reaction flask was heated up to (87 ± 2) °C by reflux and stirred at 400 rpm. A 0.5-M aqueous solution of $Fe^{2+}$ and $Fe^{3+}$ in a molar ratio of 1:2 was added to the ammonia solution until pH 10 was reached. The reaction was carried out for 1 h at (87 ± 2) °C. Instantly, when the two solutions were mixed, a dark-brown precipitate of magnetic phase was formed. After the reaction, the dark-brown $\gamma Fe_2O_3$ precipitate was separated from the supernatant by settling on the permanent magnet and rinsed with deionized water several times. Finally, the rinsed precipitate was dried in a laboratory oven at 90 °C for 24 h.

#### 3.1.2. $CoFe_2O_4$ NPs

For the synthesis of $CoFe_2O_4$ NPs, stock solutions containing $Co^{2+}$ and $Fe^{3+}$ ions were prepared using $CoCl_2{\cdot}6H_2O$ and $FeCl_3{\cdot}6H_2O$ as source materials. Stoichiometric amounts of the appropriate chlorides were dissolved in deionized water. The concentration of the solution was 0.5 M in all experiments, referred to as chloride concentration. The solution was then hydrolyzed in a 0.5-M aqueous solution of sodium hydroxide preheated to (87 ± 2) °C by reflux and stirred at 400 rpm. The reaction was carried out for 1 h at pH 10. After the reaction was completed, the dark-brown $CoFe_2O_4$ precipitate was separated from the supernatant by settling on the permanent magnet and rinsed with deionized water. The rinsing procedure was repeated several times, and the rinsed precipitate was finally dried in a laboratory oven at 90 °C for 24 h.

#### 3.1.3. $\gamma$-$Fe_2O_3$@$SiO_2$-$NH_2$ and $CoFe_2O_4$@$SiO_2$-$NH_2$ NPs

For the in situ preparation of $\gamma$-$Fe_2O_3$@$SiO_2$–$NH_2$ and $CoFe_2O_4$@$SiO_2$–$NH_2$ core@shell NPs, 21.6 mol% of 2-propanol, 15.1 mol% of distilled water, 2.2 mol% of 25% $NH_4OH$ solution, 4 mL of the prepared $\gamma$-$Fe_2O_3$ or $CoFe_2O_4$ colloidal suspension with a mass concentration ($\gamma_i$) 1.035 $\pm$ 0.005 g/mL, 0.25 mol% of TEOS, and 0.36 mol% of APTMS were mixed under magnetic stirring at 500 rpm in a closed vessel for 24 h at room temperature. After the reaction finished, the sediment was rinsed several times with ethanol (96 wt.%) and distilled water. The obtained core@shell superparamagnetic NPs were separated from the supernatant by using the permanent external magnet and dried overnight in the laboratory oven at 90 °C.

The experimental procedure for this study is schematically presented in Figure 13.

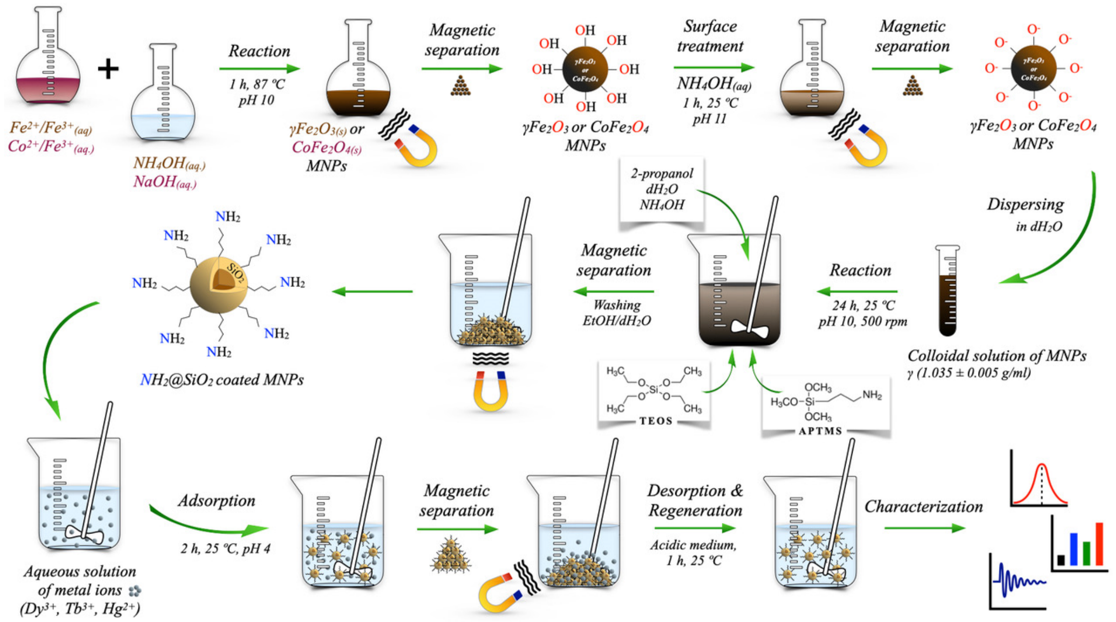


**Figure 13.** Schematic representation of the experimental procedure.

### 3.2. *Characterization of MNPs*

Prepared samples were characterized using X-ray diffractometry and transmission-electron microscopy in combination with energy-dispersive X-ray spectroscopy, Brunauer–Emmet–Teller specific-surface-area technique, Fourier-transform infrared spectroscopy, thermogravimetric analysis, electro-kinetic ($\xi$) potential measurements, inductively coupled plasma atomic emission spectroscopy, and vibrating-sample magnetometry.

#### 3.2.1. X-ray Diffractometry (XRD)

We used X-ray diffractometry (XRD) for structural analysis with a Brucker D4 Endeavor X-ray diffractometer coupled with $CuK_\alpha$ radiation (Bruker D4 Endeavor, Bruker, Billerica, MA, USA). The measurements were performed at room temperature with a time step of 30 s within the range of Bragg's angle 2 $\theta$ from 20° to 80°, with an angle step of 0.036°. The XRD utilized a Cu anode with a wavelength of 0.154 nm.

#### 3.2.2. Transmission-Electron Microscopy (TEM) with Energy-Dispersive X-ray Spectroscopy (EDXS)

The TEM images were taken using a JEOL JEM-2100 microscope, operated by drop-casting the nanoparticle suspensions on the thin carbon-coated copper grid (200 mesh, holly carbon) and drying under ambient conditions. The EDXS analyses were performed at 200 kV using a JEOL JEM-2010 microscope (JEM 2100 JEOL, JEOL Ltd., Musashino Akishima, Tokyo, Japan).

#### 3.2.3. Fourier-Transform Infrared Spectroscopy (FT-IR)

The FT-IR data were collected using a Spectrum Two FT-IR Spectrometer (PerkinElmer, Waltham, MA, USA) utilizing a KBr window for data collection over a spectral range of 400 $cm^{-1}$ to 4000 $cm^{-1}$ at a resolution of 0.5 $cm^{-1}$. The FT-IR spectra were recorded with PerkinElmer's Spectrum 10™ software at room temperature in the transmittance mode.

#### 3.2.4. Brunauer–Emmet–Teller Method (BET)

The BET was used to determine the specific surface areas of NPs by using Micromeritics, Flow Prep 060, with Tristar II 3020 (Micromeritics Instrument Corporation, Norcross, GA, USA). All samples were degassed at 110 °C for 24 h prior to each measurement. The specific surface area was measured in the 0.05–0.3 range of relative pressure in nitrogen gas at a temperature of 77.35 K after 24 h.

#### 3.2.5. Thermogravimetric Analysis (TGA)

To predict the thermal stability and chemical degradation of the functional groups grafted to the surfaces of the NPs, a TGA analysis was performed using a PerkinElmer TGA4000 thermogravimetric analyzer (PerkinElmer, Waltham, MA, USA) calibrated with nickel and iron as Curie-point-reference materials.

For the experiments, prepared powdered sample specimens were placed in a corundum ceramic sample pan, and the weights of these specimens ranged between 2 mg and 50 mg. The experiments were conducted by continuously monitoring the mass of a sample in nitrogen purge gas at a flow rate of 20 mL/min and a heating rate of 10 °C/min over a temperature range of 30 °C to 900 °C, and were controlled by PerkinElmer's thermal software Pyris Software™ version 10.1.

#### 3.2.6. Electro-Kinetic (ξ)-Potential Measurements

Dynamic light scattering was used to determine electro-kinetic phenomena, which involve the interrelation between mechanical and electrical effects at a moving interface. Electro-kinetic results were expressed in terms of ζ-potential, determined from electrophoretic mobility of particles through a field with known strength, and the term of isoelectric point (IEP), referring to the conditions under which the ζ-potential is zero. When pH is equal to or close to the isoelectric point, NPs tend to be unstable, form clusters, and precipitate. The ζ-potential was measured by ZetaSizer Nanoseries Malvern Instruments (Malvern Panalytical Ltd., Spectris Group, London, UK). Aqueous solutions of NaOH and HCl were employed to adjust the pH values of suspensions. All measurements were performed at room temperature.

#### 3.2.7. Potentiometric Titration

The pH potentiometric titrations were used for the determination of the total charge of aqueous colloidal dispersions of MNPs. The titrations were carried out in forward (acidic-to-alkaline) and backward (alkaline-to-acidic) directions at $2.5 < pH < 11.0$ using 0.1-M-HCl and 0.1-M-KOH aqueous solutions as titrants. A two-burette instrument, Mettler T-70 (Mettler Toledo, Columbus, OH, USA), was used. It was equipped with a combined glass-electrode Mettler T DG 117. The burettes were filled with 0.1 M HCl and 0.1 M KOH. All the solutions were prepared with distilled $H_2O$ with a carbonate content $<10^{-6}$ mol/L, which was achieved through boiling and consequent cooling in a nitrogen atmosphere.

Prior to the titration, the ionic strength was adjusted to an approximate value of 0.1 mol/L by the addition of a 3-M-KCl aqueous solution and then maintained constantly within 2% of the initial value upon the addition of HCl and KOH solutions.

The samples were titrated in forward and backward runs between pH 2 and pH 11. After each addition, the volume of the titration reagent was read when the equilibrium condition <0.1 mV/min was reached or the condition of the maximum waiting time of 3 min was satisfied. The blank HCl–KOH titrations were performed under the same conditions as mentioned above [150].

The titrant volume was normalized to the mass of the titrated samples and expressed as a charge per mass Q/m (in mmol/g) vs. pH curve. The amounts of charged $NH_2$ surface groups in the products were expressed in mmol/g sample. The determination of the amount of charged functional groups is described in detail elsewhere [90,150,151].

#### 3.2.8. Vibrating-Sample Magnetometry (VSM)

For magnetization measurements, a Lake Shore 7400 vibrating-sample magnetometer was used (Lake Shore Cryotronics, Inc, Westerville, OH, USA). The mass magnetization $M$ (emu/g) as a function of the applied magnetic field $H$ (Oe) was measured at room temperature for all the prepared samples.

### *3.3. Adsorption and Desorption Tests for $Dy^{3+}$, $Tb^{3+}$ and $Hg^{2+}$ Ions*

To evaluate the affinity of $Dy^{3+}$, $Tb^{3+}$, and $Hg^{2+}$ ions to the surfaces of the prepared $\gamma Fe_2O_3@SiO_2–NH_2$ and $CoFe_2O_4@SiO_2–NH_2$ adsorbent NPs, 20 mL of 10-mM standard aqueous solutions was prepared from $TbCl_3·6H_2O$, $Dy(NO_3)_3·5H_2O$, and $Hg(NO_3)_2·H_2O$ at pH 4 and temperature of 25 °C.

The adsorption study was performed by separate mixing of 50 mg $\gamma Fe_2O_3@SiO_2$-$NH_2$ and $CoFe_2O_4@SiO_2–NH_2$ adsorbents with the prepared aqueous solutions of $Dy^{3+}$, $Tb^{3+}$, and $Hg^{2+}$ ions with a concentration of 10 mM at a temperature of 25 ºC, for an adsorption time of 2 h. After the adsorption of $Dy^{3+}$, $Tb^{3+}$, and $Hg^{2+}$ ions, the magnetic adsorbents were removed from aqueous solutions with an external permanent magnet. To determine the adsorption efficiency and capacity, the ICP-OES method was used (ICP-OES, SPECTRO CITROS VISION, SPECTRO Analytical Instruments GmbH, Kleve, Germany).

The adsorption capacity $q_{ads}$, mass (mg) of adsorbed $Dy^{3+}$, $Tb^{3+}$, and $Hg^{2+}$ ions per mass (g) of $\gamma Fe_2O_3@SiO_2–NH_2$ or $CoFe_2O_4@SiO_2–NH_2$ adsorbents and adsorption efficiency $q_{ads,\%}$ were calculated by the following equations:

$$q_{ads} = \frac{(c_{ads,0} - c_{ads,e}) \cdot M_{ads} \cdot V}{m_{ads}} \left(\frac{mg}{g}\right) \quad (4)$$

$$q_{ads,\%} = \frac{c_{ads,0} - c_{ads,e}}{c_{ads,0}} \ (\%) \quad (5)$$

where $c_{ads,0}$ (mol/L) and $c_{ads,e}$ (mol/L) relate to the initial and equilibrium concentrations of $Dy^{3+}$, $Tb^{3+}$, and $Hg^{2+}$ ions, respectively, $V$ (L) denotes the solution volume, $M_{ads}$ (g/mol) is the molar mass of adsorbate, and $m_{ads}$ (g) is the mass of adsorbent NPs.

Furthermore, desorption of adsorbed $Dy^{3+}$, $Tb^{3+}$, and $Hg^{2+}$ ions from $\gamma Fe_2O_3@SiO_2–NH_2$ and $CoFe_2O_4@SiO_2–NH_2$ adsorbent surfaces was performed by mixing adsorbents with the prepared 1-M aqueous solution of $HNO_3$ at 25 °C for 1 h. Desorption capacity was determined using the ICP-OES method and calculated by Equation (6):

$$q_{des,\%} = \frac{c_{des}}{c_{ads}} \cdot 100 \ (\%) \quad (6)$$

where $c_{des}$ (mg/g) is the concentration of adsorbate desorbed and $c_{ads}$ (mg/g) is the concentration of adsorbate adsorbed. Results for adsorption and desorption of $Dy^{3+}$, $Tb^{3+}$, and $Hg^{2+}$ ions are shown in Table 1.

### *3.4. Toxicity Study of MNPs*

#### 3.4.1. Cell Cultures

Four different types of healthy cell were used; human-skeletal-muscle-derived cells (SKMDCs), human fibroblasts, murine macrophage cells (RAW264.7), and human-umbilical-vein endothelial cells (HUVECs).

The SKMDCs were maintained in an F-10 nutrient medium supplemented with 25% fetal bovine serum (FBS), 1% penicillin/streptomycin (P/S), 0.1% insulin, 0.01% fibroblast-growth factor (FGF), and 0.01% epidermal growth factor (EGF). Fibroblasts were maintained in RPMI medium supplemented with 10% FBS and 1% P/S. The RAW264.7 cells were maintained in Dulbecco's Modified Eagle's Medium (DMEM) supplemented with 10% FBS and 1% P/S. The HUVECs were maintained in Endothelial cell Growth Medium 2 supplemented with FBS (2%), EGF (5 ng/mL), basic FGF (10 ng/mL), insulin-like growth factor (ILGF) (20 ng/mL), vascular endothelial growth factor (VEGF) (0.5 ng/mL), ascorbic acid (1 μg/mL), heparin (22.5 μg/mL), and hydrocortisone (0.2 μg/mL), 1% P/S. All cell types were allowed to grow in a humidified atmosphere at 37 °C under 5% $CO_2$.

#### 3.4.2. Cytotoxicity Study

For cell-viability experiments, cells were seeded in a 96-well plate in 200 μL of their respective culture media; 24 h after cell growth, cells were treated with different concentrations of NPs and incubated for 3 days. Control cells were treated with the vehicle. After the incubation time, cells were incubated for 4 h with 0.5 mg $mL^{-1}$ of 3-(4,5-dimethylthiazol-2-yl)-2,5-diphenyltetrazoliumbromide (MTT). After MTT incubation, MTT/medium was removed, and the precipitated violet crystals were dissolved in ethanol/DMSO (1:1, *v:v*) solution with shaking for 20 min. The absorbance was measured at 540 nm. The percentage (%) of live cells was calculated as $Ab_{test}/Ab_{control}$ 100. The experiment was performed three times.

#### 3.4.3. In Vitro Hemolytic Studies

Human-blood samples were obtained from a local blood bank (Établissement Français du Sang, Occitanie, France). Blood samples were collected in lithium heparin and stored at 4 °C until use. In total, 10 mL of blood were centrifuged at 1500 rpm for 5 min, after which the obtained platelet-poor plasma (PPP) was removed (~5 mL). The blood pellet was washed with 5 mL of phosphate-buffered saline (PBS) and mixed by inversion followed by centrifugation at 1500 rpm for 5 min, a process that was repeated 5 times.

The obtained red blood cells (RBCs) were diluted with PBS (1:10, *v/v*), and then treated with nanoparticles at concentrations ranging from 0 to 500 μg/mL, after which they were incubated at 37 °C for 1 h. The positive controls were RBCs treated with 1% Triton X-100, and the negative control was PBS (diluent). After incubation, samples were centrifuged at 1500 rpm for 5 min and the obtained supernatant was transferred to a polystyrene 96-well plate for reading at 540 nm, corresponding to the free hemoglobin band, using Thermo Scientific™ Multiskan SkyHigh Microplate Spectrophotometer. The hemolysis percentage was calculated as = ($OD_{test} - OD_{PBS}/OD_{positive\ control} - OD_{PBS}$) × 100, where OD is the optical density.

#### 3.4.4. Toxicity in Zebrafish Embryos

Fertilized wild-type AB zebrafish embryos were obtained from the laboratory facility of molecular mechanisms in neurodegenerative dementia (MMDN), Inserm U1198, Montpellier University, collected and maintained at 28 °C and 14-h-light/10-h-dark cycle.

At 7 h post-fertilization (hpf), embryos were examined under the microscope, and only embryos that developed normally were selected for the study. The 7 hpf embryos (15 per group) were placed in 12-well plates and exposed to 4 mL of water containing 0, 10, 50, 125, and 500 mg/L NPs. The exposure to NPs started at 7 hpf and ended at 96 hpf. The percentages of survival, mortality, and hatching of embryos were recorded using ZEISS Stemi 508 stereo microscope (ZEISS International, Oberkochen, Germany) at 24, 48, 52, 56, 72, and 96 hpf. The experiment was performed twice.

## 4. Conclusions

Superparamagnetic $\gamma Fe_2O_3@SiO_2–NH_2$ and $CoFe_2O_4@SiO_2–NH_2$ core@shell crystalline NPs were synthesized in a simple manner using two different approaches the classical coprecipitation method and the sol-gel technique, to obtain functionalized nanosized superparamagnetic adsorbents designed for the binding and recycling of $Dy^{3+}$, $Tb^{3+}$, and $Hg^{2+}$ ions from aqueous solutions. The synthesized spherical superparamagnetic

$\gamma Fe_2O_3@SiO_2–NH_2$ and $CoFe_2O_4@SiO_2–NH_2$ NPs have excellent characteristics related to their structural, morphological, and surface properties, as well as their thermal stability, functionality, electrokinetic charge, and magnetic responsiveness. These properties were confirmed by TEM/HRTEM/EDXS, FT-IR, XRD, TGA, BET, DLS, and VSM.

Each individual material phase in the prepared $\gamma Fe_2O_3@SiO_2–NH_2$ and $CoFe_2O_4@SiO_2–NH_2$ adsorbent NPs plays a significant role in the adsorption processes. The superparamagnetic $\gamma Fe_2O_3$ and $CoFe_2O_4$ monodomain cores give the adsorbents the necessary magnetic properties and magnetic response in an external magnetic field, while the $SiO_2$ amorphous shell allows the magnetic cores to be chemically and thermally stable and, due to the high content of hydroxyl groups on its surfaces, allows the high-density grafting of amino functional groups, which is necessary for interactions with metal ions. As $Dy^{3+}$ and $Tb^{3+}$ preferentially react with amino groups, unlike $Hg^{2+}$, APTMS allows a higher capacity for their adsorption. The maximum adsorption capacities of $Dy^{3+}$, $Tb^{3+}$, and $Hg^{2+}$ ions by the $\gamma Fe_2O_3@SiO_2–NH_2$ are 4.0 mg/g, 4.7 mg/g, and 2.1 mg/g, respectively, and 4.7 mg/g, 6.2 mg/g, and 1.2 mg/g by the $CoFe_2O_4@SiO_2–NH_2$. These values were obtained with a mass adsorbate of 50 mg, a contact time of 120 min, an initial concentration of $Dy^{3+}$, $Tb^{3+}$, and $Hg^{2+}$ ions of $2 \times 10^{-6}$ mol/L, and a temperature of 25 °C. The adsorption efficiency toward the $Dy^{3+}$, $Tb^{3+}$, and $Hg^{2+}$ ions ranged from 83% to 98% for both the $\gamma Fe_2O_3@SiO_2–NH_2$ and the $CoFe_2O_4@SiO_2–NH_2$. In the post-adsorption treatment of the $\gamma Fe_2O_3@SiO_2–NH_2$ and $CoFe_2O_4@SiO_2–NH_2$ adsorbents in an acidic medium at pH 4.5, the $Dy^{3+}$, $Tb^{3+}$, and $Hg^{2+}$ ions were completely desorbed from their surfaces. The desorption efficiency was 100%.

The toxicity assessment of the prepared adsorbents provided information on the relationship between their minimum dose and their responses to adverse effects on SKMDCs, fibroblasts, RAW264.7, and HUVECs, under the expected exposure conditions. The results showed the low toxicity of all the nanoparticles in the fibroblasts; however, higher toxicity was observed in macrophage RAW264.7 cells treated with $\gamma Fe_2O_3@SiO_2–NH_2$ and $CoFe_2O_4@SiO_2–NH_2$. The recording of the survival, mortality, and hatching percentages of zebrafish embryos exposed to different concentrations of the nanoparticles showed no toxicity compared to the control until 96 hpf, even at a high adsorbent concentration of 500 mg/L.

**Supplementary Materials:** The following supporting information can be downloaded at: https://www.mdpi.com/article/10.3390/ijms241210072/s1.

**Author Contributions:** Conceptualization, A.L., J.-O.D. and A.K.; methodology: A.F.P.A.M.R., M.B., J.-O.D. and A.K.; formal analysis, A.F.P.A.M.R., L.M.A.A., M.O., M.G.-B. and A.K.; investigation, A.F.P.A.M.R., M.B., L.M.A.A., M.O., M.G.-B., J.-O.D. and A.K.; writing—original draft preparation, A.F.P.A.M.R. and A.K.; writing—review and editing, A.F.P.A.M.R., J.-O.D., L.M.A.A. and A.K.; visualization, A.F.P.A.M.R. and A.K.; supervision, A.K.; project administration, A.L.; funding acquisition, N.D. and A.L. All authors have read and agreed to the published version of the manuscript.

**Funding:** The project HMRecycle (E! 113543) received funding from the Eurostars-2 joint program. We express our gratitude to the national funding organization, Slovenian Ministry of Economic Development and Technology (MEDT), for co-financing the project HMRecycle. The work was also supported by the international research project, the Marie Skłodowska-Curie Action "Global Mercury Observation and Training Network in Support to the Minamata Convention," financed under the funding line "excellent science" of the Horizon 2020 research-and-innovation program of the European Commission, under the Marie Sklodowska-Curie grant agreement no. 860497. The results were created within the Research program Design of new properties of (nano)materials and applications, no. P2-0424, and the authors acknowledge the financial support from the Slovenian Research Agency. This research was also funded by the Ministry of Education, Science and Sport of the Republic of Slovenia and the European Union, the European, t Regional Development Fund (ERDF), and Early Research Career 2.1 (contract no. C3330-19-952032).

**Institutional Review Board Statement:** Not applicable.

**Informed Consent Statement:** Not applicable.

**Data Availability Statement:** No such data that were created with the scope to share it publically.

**Acknowledgments:** All authors would like to thank Nicolas Cubedo for providing zebrafish embryos. The author sincerely acknowledges the efforts of Matej Bračič for performing potentiometric titrations, Tjaša Kraševec Glaser B.Sc. for DLS measurements, and Nadir Bettache for the Hemolysis measurement.

**Conflicts of Interest:** The authors declare that there is no conflict of interest.

## References

1. European Commission. COM(2020) 474 COM(2020) 474: Critical Raw Materials Resilience: Charting a Path towards Greater Security and Sustainability. 2020. Available online: https://eur-lex.europa.eu/legal-content/EN/TXT/?uri=CELEX:52020DC0474 (accessed on 31 March 2023).
2. Valko, M.; Morris, H.; Cronin, M.T.D. Metals, Toxicity and Oxidative Stress. *Curr. Med. Chem.* **2005**, *12*, 1161–1208. [CrossRef] [PubMed]
3. Crans, D.C.; Kostenkova, K. Open questions on the biological roles of first-row transition metals. *Commun. Chem.* **2020**, *3*, 1–4. [CrossRef] [PubMed]
4. De Granda-Orive, J.I.; García-Quero, C. E-waste: Rare earth elements, new toxic substances in cigarettes and electronic cigarettes. *Arch. Bronconeumol.* **2020**, *56*, 477–478. [CrossRef] [PubMed]
5. Tchounwou, P.B.; Yedjou, C.G.; Patlolla, A.K.; Sutton, D.J. Heavy Metals Toxicity and the Environment. *EXS* **2012**, *101*, 133–164. [CrossRef] [PubMed]
6. Jaishankar, M.; Tseten, T.; Anbalagan, N.; Mathew, B.B.; Beeregowda, K.N. Toxicity, mechanism and health effects of some heavy metals. *Interdiscip. Toxicol.* **2014**, *7*, 60–72. [CrossRef]
7. Baughman, T.A. Elemental mercury spills. *Environ. Health Perspect.* **2006**, *114*, 147–152. [CrossRef]
8. Blengini, G.A.; Nuss, P.; Dewulf, J.; Nita, V.; Talens Peiró, L.; Vidal-Legaz, B.; Latunussa, C.; Mancini, L.; Blagoeva, D.; Pennington, D.; et al. EU methodology for critical raw materials assessment: Policy needs and proposed solutions for incremental improvements. *Resour. Policy* **2017**, *53*, 12–19. [CrossRef]
9. Gislev, M.; Grohol, M. *European Commission: Report on Critical Raw Materials and the Circular Economy*; Publications Office of the European Union: Luxembourg, 2018. [CrossRef]
10. Azimi, G.; Forsberg, K.; Ouchi, T.; Kim, H.; Alam, S.; Baba, A.A. *Rare Metal Technology 2020*; Springer International Publishing: Cham, Switzerland, 2020. [CrossRef]
11. Cui, J.; Forssberg, E. Mechanical recycling of waste electric and electronic equipment: A review. *J. Hazard. Mater.* **2003**, *99*, 243–263. [CrossRef]
12. Cui, J.; Zhang, L. Metallurgical recovery of metals from electronic waste: A review. *J. Hazard. Mater.* **2008**, *158*, 228–256. [CrossRef]
13. Birloaga, I.; Vegliò, F. Simulation and economic analysis of a hydrometallurgical approach developed for the treatment of waste printed circuit boards (WPCB). *Glob. Nest J.* **2018**, *20*, 695–699. [CrossRef]
14. Cui, J.; Roven, H.J. *Electronic Waste*; Elsevier Inc.: Amsterdam, The Netherlands, 2011. [CrossRef]
15. Ebin, B.; Isik, M.I. *Pyrometallurgical Processes for the Recovery of Metals from WEEE*; Elsevier Inc.: Amsterdam, The Netherlands, 2016. [CrossRef]
16. Zhang, J.; Anawati, J.; Yao, Y.; Azimi, G. Aeriometallurgical Extraction of Rare Earth Elements from a NdFeB Magnet Utilizing Supercritical Fluids. *ACS Sustain. Chem. Eng.* **2018**, *6*, 16713–16725. [CrossRef]
17. Gupta, C.K. *Chemical Metallurgy: Principles and Practice*; Wiley-VCH: Weinheim, Germany, 2003.
18. Tan, Q.; Li, J. Rare earth metal recovery from typical e-waste. In *Waste Electrical and Electronic Equipment (WEEE) Handbook*; Elsevier: Amsterdam, The Netherlands, 2019; pp. 393–421. [CrossRef]
19. Jowitt, S.M.; Werner, T.T.; Weng, Z.; Mudd, G.M. Recycling of the rare earth elements. *Curr. Opin. Green Sustain. Chem.* **2018**, *13*, 1–7. [CrossRef]
20. Mezy, A.; Vardanyan, A.; Garcia, A.; Schmitt, C.; Lakić, M.; Krajnc, S.; Daniel, G.; Košak, A.; Lobnik, A.; Seisenbaeva, G.A. Long-chain ligand design in creating magnetic nano adsorbents for separation of REE from LTM. *Sep. Purif. Technol.* **2021**, *276*, 119340. [CrossRef]
21. Eldridge, D.S.; Crawford, R.J.; Harding, I.H. The role of metal ion-ligand interactions during divalent metal ion adsorption. *J. Colloid Interface Sci.* **2015**, *454*, 20–26. [CrossRef] [PubMed]
22. Kampalanonwat, P.; Supaphol, P. The study of competitive adsorption of heavy metal ions from aqueous solution by aminated polyacrylonitrile nanofiber mats. In *Energy Procedia*; Elsevier Ltd.: Amsterdam, The Netherlands, 2014; pp. 142–151. [CrossRef]
23. Das, R.; Vecitis, C.D.; Schulze, A.; Cao, B.; Ismail, A.F.; Lu, X.; Chen, J.; Ramakrishna, S. Recent advances in nanomaterials for water protection and monitoring. *Chem. Soc. Rev.* **2017**, *46*, 6946–7020. [CrossRef]
24. Simeonidis, K.; Mourdikoudis, S.; Kaprara, E.; Mitrakas, M.; Polavarapu, L. Inorganic engineered nanoparticles in drinking water treatment: A critical review. *Environ. Sci. Water Res. Technol.* **2016**, *2*, 43–70. [CrossRef]
25. Leonel, A.G.; Mansur, A.A.P.; Mansur, H.S. Advanced Functional Nanostructures based on Magnetic Iron Oxide Nanomaterials for Water Remediation: A Review. *Water Res.* **2021**, *190*. [CrossRef]

26. Hao, L.; Liu, M.; Wang, N.; Li, G. A critical review on arsenic removal from water using iron-based adsorbents. *RSC Adv.* **2018**, *8*, 39545–39560. [CrossRef]
27. Reddy, L.H.; Arias, J.L.; Nicolas, J.; Couvreur, P. Magnetic nanoparticles: Design and characterization, toxicity and biocompatibility, pharmaceutical and biomedical applications. *Chem. Rev.* **2012**, *112*, 5818–5878. [CrossRef]
28. Laurent, S.; Forge, D.; Port, M.; Roch, A.; Robic, C.; Vander Elst, L.; Muller, R.N. Magnetic iron oxide nanoparticles: Synthesis, stabilization, vectorization, physicochemical characterizations and biological applications. *Chem. Rev.* **2008**, *108*, 2064–2110. [CrossRef]
29. Durán, J.D.G.; Arias, J.L.; Gallardo, V.; Delgado, A.V. Magnetic colloids as drug vehicles. *J. Pharm. Sci.* **2008**, *97*, 2948–2983. [CrossRef]
30. Rehman, A.U.; Nazir, S.; Irshad, R.; Tahir, K.; ur Rehman, K.; Islam, R.U.; Wahab, Z. Toxicity of heavy metals in plants and animals and their uptake by magnetic iron oxide nanoparticles. *J. Mol. Liq.* **2021**, *321*, 114455. [CrossRef]
31. Hadela, A.; Lakić, M.; Potočnik, M.; Košak, A.; Gutmaher, A.; Lobnik, A. Novel reusable functionalized magnetic cobalt ferrite nanoparticles as oil adsorbents. *Adsorpt. Sci. Technol.* **2020**, *38*, 168–190. [CrossRef]
32. Li, F.; Gong, A.; Qiu, L.; Zhang, W.; Li, J.; Liu, Z. Diglycolamide-grafted Fe3O4/polydopamine nanomaterial as a novel magnetic adsorbent for preconcentration of rare earth elements in water samples prior to inductively coupled plasma optical emission spectrometry determination. *Chem. Eng. J.* **2019**, *361*, 1098–1109. [CrossRef]
33. Sumit, W.A. Superparamagnetic iron oxide nanoparticles: Magnetic nanoplatforms as drug carriers. *Int. J. Nanomed.* **2012**, *7*, 3445–3471. [CrossRef]
34. Liu, X.M.; Yang, G.; Fu, S.Y. Mass synthesis of nanocrystalline spinel ferrites by a polymer-pyrolysis route. *Mater. Sci. Eng. C* **2007**, *27*, 750–755. [CrossRef]
35. Koroteev, P.S.; Dobrokhotova, Z.V.; Grechnikov, F.V.; Novotortsev, V.M. Heterometallic Carboxylate Complexes as Precursors for Mixed Oxides: II. d–d Carboxylates. *Russ. J. Gen. Chem.* **2018**, *88*, 1290–1305. [CrossRef]
36. Sajjia, M.; Baroutaji, A.; Olabi, A.G. The Introduction of Cobalt Ferrite Nanoparticles as a Solution for Magnetostrictive Applications. In *Reference Module in Materials Science and Materials Engineering*; Elsevier: Amsterdam, The Netherlands, 2017. [CrossRef]
37. Saddeler, S.; Bendt, G.; Salamon, S.; Haase, F.T.; Landers, J.; Timoshenko, J.; Rettenmaier, C.; Jeon, H.S.; Bergmann, A.; Wende, H.; et al. Influence of the cobalt content in cobalt iron oxides on the electrocatalytic OER activity. *J. Mater. Chem. A* **2021**, *9*, 25381–25390. [CrossRef]
38. Mozaffari, M.; Hadadian, Y.; Aftabi, A.; Oveisy Moakhar, M. The effect of cobalt substitution on magnetic hardening of magnetite. *J. Magn. Magn. Mater.* **2014**, *354*, 119–124. [CrossRef]
39. Slonczewski, J.C. Origin of Magnetic Anisotropy in Cobalt-Substituted Magnetite*. *Phys. Rev.* **1958**, *110*, 1341–1348. [CrossRef]
40. Prado, Y.; Daffé, N.; Michel, A.; Georgelin, T.; Yaacoub, N.; Grenèche, J.M.; Choueikani, F.; Otero, E.; Ohresser, P.; Arrio, M.A.; et al. Enhancing the magnetic anisotropy of maghemite nanoparticles via the surface coordination of molecular complexes. *Nat. Commun.* **2015**, *6*, 10139. [CrossRef] [PubMed]
41. Cypriyana, P.J.J.; Saigeetha, S.; Angalene, J.L.A.; Samrot, A.V.; Kumar, S.S.; Ponniah, P.; Chakravarthi, S. Overview on toxicity of nanoparticles, it's mechanism, models used in toxicity studies and disposal methods—A review. *Biocatal. Agric. Biotechnol.* **2021**, *36*, 102117. [CrossRef]
42. Khanna, R.; Mukherjee, P.S.; Park, M. A critical assessment on resource recovery from electronic waste: Impact of mechanical pre-treatment. *J. Clean. Prod.* **2020**, *268*, 122319. [CrossRef]
43. Devasena, T.; Iffath, B.; Renjith Kumar, R.; Muninathan, N.; Baskaran, K.; Srinivasan, T.; John, S.T. Insights on the Dynamics and Toxicity of Nanoparticles in Environmental Matrices. *Bioinorg. Chem. Appl.* **2022**, *2022*, 1–21. [CrossRef] [PubMed]
44. Singh, N.; Jenkins, G.J.S.; Asadi, R.; Doak, S.H. Potential toxicity of superparamagnetic iron oxide nanoparticles (SPION). *Nano Rev.* **2010**, *1*, 5358. [CrossRef]
45. Zhu, X.; Tian, S.; Cai, Z. Toxicity Assessment of Iron Oxide Nanoparticles in Zebrafish (*Danio rerio*) Early Life Stages. *PLoS ONE* **2012**, *7*, e46286. [CrossRef]
46. Seisenbaeva, G.A.; Ali, L.M.A.; Vardanyan, A.; Gary-Bobo, M.; Budnyak, T.M.; Kessler, V.G.; Durand, J.O. Mesoporous silica adsorbents modified with amino polycarboxylate ligands—Functional characteristics, health and environmental effects. *J. Hazard. Mater.* **2021**, *406*, 124698. [CrossRef]
47. Kim, J.S.; Yoon, T.J.; Yu, K.N.; Kim, B.G.; Park, S.J.; Kim, H.W.; Lee, K.H.; Park, S.B.; Lee, J.K.; Cho, M.H. Toxicity and tissue distribution of magnetic nanoparticles in mice. *Toxicol. Sci.* **2006**, *89*, 338–347. [CrossRef]
48. Hussain, S.M.; Hess, K.L.; Gearhart, J.M.; Geiss, K.T.; Schlager, J.J. In vitro toxicity of nanoparticles in BRL 3A rat liver cells. *Toxicol. In Vitro* **2005**, *19*, 975–983. [CrossRef]
49. Karlsson, H.L.; Gustafsson, J.; Cronholm, P.; Möller, L. Size-dependent toxicity of metal oxide particles-A comparison between nano- and micrometer size. *Toxicol. Lett.* **2009**, *188*, 112–118. [CrossRef]
50. Veranth, J.M.; Kaser, E.G.; Veranth, M.M.; Koch, M.; Yost, G.S. Cytokine responses of human lung cells (BEAS-2B) treated with micron-sized and nanoparticles of metal oxides compared to soil dusts. *Part. Fibre Toxicol.* **2007**, *4*, 2. [CrossRef] [PubMed]
51. Häfeli, U.O.; Riffle, J.S.; Harris-Shekhawat, L.; Carmichael-Baranauskas, A.; Mark, F.; Dailey, J.P.; Bardenstein, D. Cell uptake and in vitro toxicity of magnetic nanoparticles suitable for drug delivery. *Mol. Pharm.* **2009**, *6*, 1417–1428. [CrossRef] [PubMed]

52. Jeng, H.A.; Swanson, J. Toxicity of metal oxide nanoparticles in mammalian cells. *J. Environ. Sci. Health Part A Toxic/Hazardous Subst. Environ. Eng.* **2006**, *41*, 2699–2711. [CrossRef] [PubMed]
53. Stroh, A.; Zimmer, C.; Gutzeit, C.; Jakstadt, M.; Marschinke, F.; Jung, T.; Pilgrimm, H.; Grune, T. Iron oxide particles for molecular magnetic resonance imaging cause transient oxidative stress in rat macrophages. *Free Radic. Biol. Med.* **2004**, *36*, 976–984. [CrossRef] [PubMed]
54. Sadeghiani, N.; Barbosa, L.S.; Silva, L.P.; Azevedo, R.B.; Morais, P.C.; Lacava, Z.G.M. Genotoxicity and inflammatory investigation in mice treated with magnetite nanoparticles surface coated with polyaspartic acid. *J. Magn. Magn. Mater.* **2005**, *289*, 466–468. [CrossRef]
55. Volatron, J.; Kolosnjaj-Tabi, J.; Javed, Y.; Vuong, Q.L.; Gossuin, Y.; Neveu, S.; Luciani, N.; Hémadi, M.; Carn, F.; Alloyeau, D.; et al. Physiological Remediation of Cobalt Ferrite Nanoparticles by Ferritin. *Sci. Rep.* **2017**, *7*, 40075. [CrossRef] [PubMed]
56. Ahmad, F.; Liu, X.; Zhou, Y.; Yao, H. An in vivo evaluation of acute toxicity of cobalt ferrite ($CoFe_2O_4$) nanoparticles in larval-embryo Zebrafish (*Danio rerio*). *Aquat. Toxicol.* **2015**, *166*, 21–28. [CrossRef]
57. Ahmad, F.; Yao, H.; Zhou, Y.; Liu, X. Toxicity of cobalt ferrite ($CoFe_2O_4$) nanobeads in Chlorella vulgaris: Interaction, adaptation and oxidative stress. *Chemosphere* **2015**, *139*, 479–485. [CrossRef]
58. Horev-Azaria, L.; Baldi, G.; Beno, D.; Bonacchi, D.; Golla-Schindler, U.; Kirkpatrick, J.C.; Kolle, S.; Landsiedel, R.; Maimon, O.; Marche, P.N.; et al. Predictive Toxicology of cobalt ferrite nanoparticles: Comparative in-vitro study of different cellular models using methods of knowledge discovery from data. *Part. Fibre Toxicol.* **2013**, *10*, 32. [CrossRef]
59. Romih, T.; Drašler, B.; Jemec, A.; Drobne, D.; Novak, S.; Golobič, M.; Makovec, D.; Susič, R.; Kogej, K. Bioavailability of cobalt and iron from citric-acid-adsorbed CoFe2O4 nanoparticles in the terrestrial isopod Porcellio scaber. *Sci. Total Environ.* **2015**, *508*, 76–84. [CrossRef]
60. López-Moreno, M.L.; Avilés, L.L.; Pérez, N.G.; Irizarry, B.Á.; Perales, O.; Cedeno-Mattei, Y.; Román, F. Effect of cobalt ferrite ($CoFe_2O_4$) nanoparticles on the growth and development of Lycopersicon lycopersicum (tomato plants). *Sci. Total Environ.* **2016**, *550*, 45–52. [CrossRef] [PubMed]
61. Haneda, K.; Morrish, A.; Morrish, A.H. Magnetite to Maghemite Transformation in Ultrafine Particles. *J. Phys. Colloq.* **1977**, *38*, 321–323. [CrossRef]
62. Li, Z.; Chanéac, C.; Berger, G.; Delaunay, S.; Graff, A.; Lefèvre, G. Mechanism and kinetics of magnetite oxidation under hydrothermal conditions. *RSC Adv.* **2019**, *9*, 33633–33642. [CrossRef]
63. Malvindi, M.A.; Brunetti, V.; Vecchio, G.; Galeone, A.; Cingolani, R.; Pompa, P.P. $SiO_2$ nanoparticles biocompatibility and their potential for gene delivery and silencing. *Nanoscale* **2012**, *4*, 486–495. [CrossRef] [PubMed]
64. Bardi, G.; Malvindi, M.A.; Gherardini, L.; Costa, M.; Pompa, P.P.; Cingolani, R.; Pizzorusso, T. The biocompatibility of amino functionalized CdSe/ZnS quantum-dot-Doped $SiO_2$ nanoparticles with primary neural cells and their gene carrying performance. *Biomaterials* **2010**, *31*, 6555–6566. [CrossRef]
65. Malvindi, M.A.; De Matteis, V.; Galeone, A.; Brunetti, V.; Anyfantis, G.C.; Athanassiou, A.; Cingolani, R.; Pompa, P.P. Toxicity assessment of silica coated iron oxide nanoparticles and biocompatibility improvement by surface engineering. *PLoS ONE* **2014**, *9*, e85835. [CrossRef]
66. Juang, J.H.; Wang, J.J.; Shen, C.R.; Kuo, C.H.; Chien, Y.W.; Kuo, H.Y.; Tsai, Z.T.; Yen, T.C. Magnetic resonance imaging of transplanted mouse islets labeled with chitosan-coated superparamagnetic iron oxide nanoparticles. *Transplant. Proc.* **2010**, *42*, 2104–2108. [CrossRef]
67. Kyle, P.B. Toxicology: GCMS. In *Mass Spectrometry for the Clinical Laboratory*; Elsevier Inc.: Amsterdam, The Netherlands, 2017; pp. 131–163. [CrossRef]
68. Dupont, D.; Brullot, W.; Bloemen, M.; Verbiest, T.; Binnemans, K. Selective uptake of rare earths from aqueous solutions by EDTA-functionalized magnetic and nonmagnetic nanoparticles. *ACS Appl. Mater. Interfaces* **2014**, *6*, 4980–4988. [CrossRef]
69. Košak, A.; Bauman, M.; Padežnik-Gomilšek, J.; Lobnik, A. Lead (II) complexation with 3-mercaptopropyl-groups in the surface layer of silica nanoparticles: Sorption, kinetics and EXAFS/XANES study. *J. Mol. Liq.* **2017**, *229*, 371–379. [CrossRef]
70. Topel, S.D.; Legaria, E.P.; Tiseanu, C.; Rocha, J.; Nedelec, J.M.; Kessler, V.G.; Seisenbaeva, G.A. Hybrid silica nanoparticles for sequestration and luminescence detection of trivalent rare-earth ions ($Dy^{3+}$ and $Nd^{3+}$) in solution. *J. Nanoparticle Res.* **2014**, *16*, 1–17. [CrossRef]
71. Fröhlich, E. The role of surface charge in cellular uptake and cytotoxicity of medical nanoparticles. *Int. J. Nanomed.* **2012**, *7*, 5577–5591. [CrossRef]
72. Zhu, X.M.; Wang, Y.X.J.; Leung, K.C.F.; Lee, S.F.; Zhao, F.; Wang, D.W.; Lai, J.M.Y.; Wan, C.; Cheng, C.H.K.; Ahuja, A.T. Enhanced cellular uptake of aminosilane-coated superparamagnetic iron oxide nanoparticles in mammalian cell lines. *Int. J. Nanomed.* **2012**, *7*, 953–964. [CrossRef]
73. Sun, Z.; Yathindranath, V.; Worden, M.; Thliveris, J.A.; Chu, S.; Parkinson, F.E.; Hegmann, T.; Miller, D.W. Characterization of cellular uptake and toxicity of aminosilane-coated iron oxide nanoparticles with different charges in central nervous system-relevant cell culture models. *Int. J. Nanomed.* **2013**, *8*, 961–970. [CrossRef] [PubMed]
74. Berry, C.C.; Wells, S.; Charles, S.; Curtis, A.S.G. Dextran and albumin derivatised iron oxide nanoparticles: Influence on fibroblasts in vitro. *Biomaterials* **2003**, *24*, 4551–4557. [CrossRef] [PubMed]
75. Berry, C.C.; Wells, S.; Charles, S.; Aitchison, G.; Curtis, A.S.G. Cell response to dextran-derivatised iron oxide nanoparticles post internalisation. *Biomaterials* **2004**, *25*, 5405–5413. [CrossRef] [PubMed]

76. Wu, X.; Tan, Y.; Mao, H.; Zhang, M. Toxic effects of iron oxide nanoparticles on human umbilical vein endothelial cells. *Int. J. Nanomed.* **2010**, *5*, 385–399. [CrossRef]
77. Chen, B.A.; Jin, N.; Wang, J.; Ding, J.; Gao, C.; Cheng, J.; Xia, G.; Gao, F.; Zhou, Y.; Chen, Y.; et al. The effect of magnetic nanoparticles of Fe3O4 on immune function in normal ICR mice. *Int. J. Nanomed.* **2010**, *5*, 593–599. [CrossRef]
78. Patterson, A.L. The scherrer formula for X-ray particle size determination. *Phys. Rev.* **1939**, *56*, 978–982. [CrossRef]
79. Holzwarth, U.; Gibson, N. The Scherrer equation versus the "Debye-Scherrer equation". *Nat. Nanotechnol.* **2011**, *6*, 534. [CrossRef]
80. Viltužnik, B.; Lobnik, A.; Košak, A. The removal of Hg(II) ions from aqueous solutions by using thiol-functionalized cobalt ferrite magnetic nanoparticles. *J. Sol-Gel Sci. Technol.* **2015**, *74*, 199–207. [CrossRef]
81. Spencer, M.P.; Lee, W.; Alsaati, A.; Breznak, C.M.; Braga Nogueira Branco, R.; Dai, J.; Gomez, E.D.; Marconnet, A.; Lockette, P.; Yamamoto, N. Cold sintering to form bulk maghemite for characterization beyond magnetic properties. *Int. J. Ceram. Eng. Sci.* **2019**, *1*, 119–124. [CrossRef]
82. Rajput, A.B.; Hazra, S.; Ghosh, N.N. Synthesis and characterisation of pure single-phase CoFe2O4 nanopowder via a simple aqueous solution-based EDTA-precursor route. *J. Exp. Nanosci.* **2013**, *8*, 629–639. [CrossRef]
83. Košak, A.; Makovec, D.; Drofenik, M. Microemulsion synthesis of MnZn-ferrite nanoparticles. *Mater. Sci. Forum* **2004**, *453–454*, 219–224. [CrossRef]
84. Kegl, T.; Ban, I.; Lobnik, A.; Košak, A. Synthesis and characterization of novel Γ-$Fe_2O_3$-NH4OH@$SiO_2$(APTMS) nanoparticles for dysprosium adsorption. *J. Hazard. Mater.* **2019**, *378*, 120764. [CrossRef]
85. Wang, Q.Z.; Chen, X.G.; Liu, N.; Wang, S.X.; Liu, C.S.; Meng, X.H.; Liu, C.G. Protonation constants of chitosan with different molecular weight and degree of deacetylation. *Carbohydr. Polym.* **2006**, *65*, 194–201. [CrossRef]
86. Al-Zebari, N.; Best, S.M.; Cameron, R.E. Effects of reaction pH on self-crosslinked chitosan-carrageenan polyelectrolyte complex gels and sponges. *J. Phys Mater.* **2019**, *2*, 15003. [CrossRef]
87. Jiang, J.; Oberdörster, G.; Biswas, P. Characterization of size, surface charge, and agglomeration state of nanoparticle dispersions for toxicological studies. *J. Nanoparticle Res.* **2009**, *11*, 77–89. [CrossRef]
88. Amornkitbamrung, L.; Mohan, T.; Hribernik, S.; Reichel, V.; Faivre, D.; Gregorova, A.; Engel, P.; Kargl, R.; Ribitsch, V. Polysaccharide stabilized nanoparticles for deacidification and strengthening of paper. *RSC Adv.* **2015**, *5*, 32950–32961. [CrossRef]
89. Elzey, S.; Grassian, V.H. Agglomeration, isolation and dissolution of commercially manufactured silver nanoparticles in aqueous environments. *J. Nanoparticle Res.* **2010**, *12*, 1945–1958. [CrossRef]
90. Bračič, M.; Mohan, T.; Griesser, T.; Stana-Kleinschek, K.; Strnad, S.; Fras-Zemljič, L. One-Step Noncovalent Surface Functionalization of PDMS with Chitosan-Based Bioparticles and Their Protein-Repellent Properties. *Adv. Mater. Interfaces* **2017**, *4*, 1700416. [CrossRef]
91. Pearson, R.G. The HSAB Principle—More quantitative aspects. *Inorg. Chim. Acta* **1995**, *240*, 93–98. [CrossRef]
92. Parr, R.G.; Pearson, R.G. Absolute Hardness: Companion Parameter to Absolute Electronegativity. *J. Am. Chem. Soc.* **1983**, *105*, 7512–7516. [CrossRef]
93. Pearson, R.G. Absolute Electronegativity and Hardness: Application to Inorganic Chemistry. *Inorg. Chem.* **1988**, *27*, 734–740. [CrossRef]
94. Moore, C.E. *Ionization Potentials and Ionization Limits Derived from the Analyses of Optical Spectra*; U.S. Government Printing Office: Washington, DC, USA, 1970. [CrossRef]
95. Allred, A.L.; Rochow, E.G. A Scale of Electronegativity Based on Electrostatic Force. *J. Lnorg. Nucl. Chem.* **1958**, *5*, 246–268. [CrossRef]
96. Gaffney, J.; Marley, N. In-depth review of atmospheric mercury: Sources, transformations, and potential sinks. *Energy Emiss. Control Technol.* **2014**, *2*, 1–21. [CrossRef]
97. Huang, C. *Rare Earth Coordination Chemistry: Fundamentals and Applications*; John Wiley & Sons: Singapore, 2010.
98. Li, K.; Xue, D. Estimation of electronegativity values of elements in different valence states. *J. Phys. Chem. A* **2006**, *110*, 11332–11337. [CrossRef]
99. Košak, A.; Lobnik, A.; Bauman, M. Adsorption of mercury(II), lead(II), cadmium(II) and zinc(II) from aqueous solutions using mercapto-modified silica particles. *Int. J. Appl. Ceram. Technol.* **2015**, *12*, 461–472. [CrossRef]
100. Zhao, F.; Repo, E.; Song, Y.; Yin, D.; Hammouda, S.B.; Chen, L.; Kalliola, S.; Tang, J.; Tam, K.C.; Sillanpää, M. Polyethylenimine-cross-linked cellulose nanocrystals for highly efficient recovery of rare earth elements from water and a mechanism study. *Green Chem.* **2017**, *19*, 4816–4828. [CrossRef]
101. Smith, D.W. Ionic Hydration Enthalpies. *J. Chem. Educ.* **1977**, *54*, 540–542. [CrossRef]
102. Sparks, D.L. *Environmental Soil Chemistry*, 2nd ed.; Academic Press Inc.: San Diego, CA, USA, 2003.
103. Bjerrum, J. *Metal Ammine Formation in Aqueous Solution: Theory of the Reversiblestep Reactions*; P. Haase and Son: Copenhagen, Denmark, 1941.
104. Hübener, S. *Actinide Elements, Encyclopedia of Physical Science and Technology*, 3rd ed.; Academic Press: Cambridge, MA, USA, 2003. [CrossRef]
105. Muthaiah, S.; Bhatia, A.; Kannan, M. Stability of Metal Complexes. In *Stability and Applications of Coordination Compounds*; Intechopen: London, UK, 2020; pp. 1–18. [CrossRef]
106. Karroker, D.G. Coordination of Trivalent Lanthanide Ions. *J. Chem. Educ.* **1970**, *47*, 424–430. [CrossRef]

107. Beattie, J.K.; Best, S.P.; Skelton, B.W.; White, A.H. Structural studies on the caesium alums, CsMIII$[SO_4]_2 \cdot 12H_2O$. *J. Chem. Soc. Dalt. Trans.* **1981**, 2105–2111. [CrossRef]
108. Buzko, V.; Sukhno, I.; Buzko, M. Ab initio and DFT study of $Lu^{3+}$ hydration. *J. Mol. Struct. Theocem.* **2009**, *894*, 75–79. [CrossRef]
109. Persson, I. Hydrated metal ions in aqueous solution: How regular are their structures? *Pure Appl. Chem.* **2010**, *82*, 1901–1917. [CrossRef]
110. Rudolph, W.W.; Irmer, G. On the Hydration of the Rare Earth Ions in Aqueous Solution. *J. Solut. Chem.* **2020**, *49*, 316–331. [CrossRef]
111. Zhang, J.; Heinz, N.; Dolg, M. Understanding lanthanoid(III) hydration structure and kinetics by insights from energies and wave functions. *Inorg. Chem.* **2014**, *53*, 7700–7708. [CrossRef]
112. Helm, L.; Merbach, A.E. Inorganic and bioinorganic solvent exchange mechanisms. *Chem. Rev.* **2005**, *105*, 1923–1959. [CrossRef]
113. Dangelo, P.; Zitolo, A.; Migliorati, V.; Chillemi, G.; Duvail, M.; Vitorge, P.; Abadie, S.; Spezia, R. Revised ionic radii of lanthanoid(III) ions in aqueous solution. *Inorg. Chem.* **2011**, *50*, 4572–4579. [CrossRef]
114. Housecroft, C.E.; Sharpe, A.G. *Inorganic Chemistry*, 4th ed.; Pearson Education Limited: London, UK, 2012.
115. Atwood, D.A. *The Rare Earth Elements: Fundamentals and Applications*; John Wiley & Sons Ltd.: Chichester, UK, 2012.
116. Huheey, J.E. *Inorganic Chemistry, Principles of Structure and Reactivity*, 2nd ed.; Harper & Row: New York, NY, USA, 1978.
117. Partana, C.F.; Suwardi; Salim, A. Structure and dynamics of Hg2+ in aqueous solution: An Ab Initio QM/MM molecular dynamics study. *J. Phys. Conf. Ser.* **2019**, *1156*, 12012. [CrossRef]
118. Persson, I. Structures of Hydrated Metal Ions in Solid State and Aqueous Solution. *Liquids* **2022**, *2*, 210–242. [CrossRef]
119. Meyer, G.; Nockemann, P. Affinity of divalent mercury towards nitrogen donor ligands. *Zeitschrift Anorg. Allg. Chem.* **2003**, *629*, 1447–1461. [CrossRef]
120. Chen, H.; Shi, R.; Ow, H. Predicting Stability Constants for Terbium(III) Complexes with Dipicolinic Acid and 4-Substituted Dipicolinic Acid Analogues using Density Functional Theory. *ACS Omega* **2019**, *4*, 20665–20671. [CrossRef] [PubMed]
121. Patel, H. Review on solvent desorption study from exhausted adsorbent. *J. Saudi Chem. Soc.* **2021**, *25*, 101302–101313. [CrossRef]
122. Allwin Mabes Raj, A.F.P.; Bauman, M.; Lakić, M.; Dimitrušev, N.; Lobnik, A.; Košak, A. Removal of $Pb^2$+, CrT, and $Hg^2$+ Ions from Aqueous Solutions Using Amino-Functionalized Magnetic Nanoparticles. *Int. J. Mol. Sci.* **2022**, *23*, 16186. [CrossRef]
123. Raj, A.F.P.A.M.; Krajnc, S.; Bauman, M.; Lakić, M.; Gutmaher, A.; Lobnik, A.; Košak, A. Removal of $Pb^2$+, $Cr^3$+ and $Hg^2$+ ions from aqueous solutions using $SiO_2$ and amino-functionalized $SiO_2$ particles. *J. Sol-Gel Sci. Technol.* **2022**, *103*, 290–308. [CrossRef]
124. Liu, C.; Liang, X.; Liu, J.; Yuan, W. Desorption of copper ions from the polyamine-functionalized adsorbents: Behaviors and mechanisms. *Adsorpt. Sci. Technol.* **2016**, *34*, 455–468. [CrossRef]
125. Su, S.; Chen, B.; He, M.; Hu, B.; Xiao, Z. Determination of trace/ultratrace rare earth elements in environmental samples by ICP-MS after magnetic solid phase extraction with $Fe_3O_4$@$SiO_2$@polyaniline-graphene oxide composite. *Talanta* **2014**, *119*, 458–466. [CrossRef]
126. Liu, E.; Zheng, X.; Xu, X.; Zhang, F.; Liu, E.; Wang, Y.; Li, C.; Yan, Y. Preparation of diethylenetriamine-modified magnetic chitosan nanoparticles for adsorption of rare-earth metal ions. *New J. Chem.* **2017**, *41*, 7739–7750. [CrossRef]
127. Javadian, H.; Taghavi, M.; Ruiz, M.; Tyagi, I.; Farsadrooh, M.; Sastre, A.M. Adsorption of neodymium, terbium and dysprosium using a synthetic polymer-based magnetic adsorbent. *J. Rare Earths*, 2022; *in press*. [CrossRef]
128. Shinozaki, T.; Ogata, T.; Kakinuma, R.; Narita, H.; Tokoro, C.; Tanaka, M. Preparation of Polymeric Adsorbents Bearing Diglycolamic Acid Ligands for Rare Earth Elements. *Ind. Eng. Chem. Res.* **2018**, *57*, 11424–11430. [CrossRef]
129. Alcaraz, L.; Escudero, M.E.; Alguacil, F.J.; Llorente, I.; Urbieta, A.; Fernández, P.; López, F.A. Dysprosium removal fromwater using active carbons obtained from spent coffee ground. *Nanomaterials* **2019**, *9*, 1372. [CrossRef]
130. Viana, T.; Henriques, B.; Ferreira, N.; Lopes, C.; Tavares, D.; Fabre, E.; Carvalho, L.; Pinheiro-Torres, J.; Pereira, E. Sustainable recovery of neodymium and dysprosium from waters through seaweeds: Influence of operational parameters. *Chemosphere* **2021**, *280*, 130600–130612. [CrossRef] [PubMed]
131. Zhang, H.; Mcdowell, R.G.; Martin, L.R.; Qiang, Y. Selective Extraction of Heavy and Light Lanthanides from Aqueous Solution by Advanced Magnetic Nanosorbents. *ACS Appl. Mater. Interfaces* **2016**, *8*, 9523–9531. [CrossRef] [PubMed]
132. Barros, Ó.; Costa, L.; Costa, F.; Lago, A.; Rocha, V.; Vipotnik, Z.; Silva, B.; Tavares, T. Recovery of rare earth elements from wastewater towards a circular economy. *Molecules* **2019**, *24*, 1005. [CrossRef]
133. Tong, S.; Zhao, S.; Zhou, W.; Li, R.; Jia, Q. Modification of multi-walled carbon nanotubes with tannic acid for the adsorption of La, Tb and Lu ions. *Microchim. Acta* **2011**, *174*, 257–264. [CrossRef]
134. Kegl, T.; Košak, A.; Lobnik, A.; Ban, I. Terbium ion adsorption from aqueous solution by using magnetic$\gamma$-$Fe_2O_3$-NH4OH@$SiO_2$ nanoparticles functionalized with amino groups. *Materials* **2019**, *12*, 1294. [CrossRef] [PubMed]
135. Zhang, Y.; Yan, T.; Yan, L.; Guo, X.; Cui, L.; Wei, Q.; Du, B. Preparation of novel cobalt ferrite/chitosan grafted with graphene composite as effective adsorbents for mercury ions. *J. Mol. Liq.* **2014**, *198*, 381–387. [CrossRef]
136. Lin, Z.; Pan, Z.; Zhao, Y.; Qian, L.; Shen, J.; Xia, K.; Guo, Y.; Qu, Z. Removal of Hg2+ with polypyrrole-functionalized Fe3O4/kaolin: Synthesis, performance and optimization with response surface methodology. *Nanomaterials* **2020**, *10*, 1370. [CrossRef]
137. Wang, X.; Zhang, Z.; Zhao, Y.; Xia, K.; Guo, Y.; Qu, Z.; Bai, R. A mild and facile synthesis of amino functionalized $CoFe_2O_4$ @$SiO_2$ for Hg(II) removal. *Nanomaterials* **2018**, *8*, 673. [CrossRef]
138. Xia, K.; Guo, Y.; Shao, Q.; Zan, Q.; Bai, R. Removal of mercury (II) by EDTA-functionalized magnetic $CoFe_2O_4$@$SiO_2$ nanomaterial with core-shell structure. *Nanomaterials* **2019**, *9*, 1532. [CrossRef]

139. Inglezakis, V.J.; Kurbanova, A.; Molkenova, A.; Zorpas, A.A.; Atabaev, T.S. Magnetic $Fe_3O_4$-Ag0 nanocomposites for effective mercury removal from water. *Sustainability* **2020**, *12*, 5489. [CrossRef]
140. Liu, Z.; Sun, Y.; Xu, X.; Qu, J.; Qu, B. Adsorption of Hg(II) in an Aqueous Solution by Activated Carbon Prepared from Rice Husk Using KOH Activation. *ACS Omega* **2020**, *5*, 29231–29242. [CrossRef] [PubMed]
141. Denizli, A.; Dem Arpa, I.V.; Bektas, S.; Genç, Ö. Adsorption of Mercury(II) Ions on Procion Blue MX-3G-attached Magnetic Poly(vinyl alcohol) Gel Beads. *Adsorpt. Sci. Technol.* **2002**, *20*, 91–106. [CrossRef]
142. Solis, K.L.; Nam, G.U.; Hong, Y. Effectiveness of gold nanoparticle-coated silica in the removal of inorganic mercury in aqueous systems: Equilibrium and kinetic studies. *Environ. Eng. Res.* **2016**, *21*, 99–107. [CrossRef]
143. Shim, W.; Paik, M.J.; Nguyen, D.T.; Lee, J.K.; Lee, Y.; Kim, J.H.; Shin, E.H.; Kang, J.S.; Jung, H.S.; Choi, S.; et al. Analysis of changes in gene expression and metabolic profiles induced by silica-coated magnetic nanoparticles. *ACS Nano* **2012**, *6*, 7665–7680. [CrossRef] [PubMed]
144. Pisani, C.; Gaillard, J.C.; Nouvel, V.; Odorico, M.; Armengaud, J.; Prat, O. High-throughput, quantitative assessment of the effects of low-dose silica nanoparticles on lung cells: Grasping complex toxicity with a great depth of field. *BMC Genom.* **2015**, *16*, 315. [CrossRef]
145. Ellinger-Ziegelbauer, H.; Pauluhn, J. Pulmonary toxicity of multi-walled carbon nanotubes (Baytubes®) relative to α-quartz following a single 6 h inhalation exposure of rats and a 3 months post-exposure period. *Toxicology* **2009**, *266*, 16–29. [CrossRef]
146. Jovanović, B.; Ji, T.; Palić, D. Gene expression of zebrafish embryos exposed to titanium dioxide nanoparticles and hydroxylated fullerenes. *Ecotoxicol. Environ. Saf.* **2011**, *74*, 1518–1525. [CrossRef]
147. Böhmert, L.; Niemann, B.; Lichtenstein, D.; Juling, S.; Lampen, A. Molecular mechanism of silver nanoparticles in human intestinal cells. *Nanotoxicology* **2015**, *9*, 852–860. [CrossRef]
148. Conde, J.; Larguinho, M.; Cordeiro, A.; Raposo, L.R.; Costa, P.M.; Santos, S.; Diniz, M.S.; Fernandes, A.R.; Baptista, P.V. Gold-nanobeacons for gene therapy: Evaluation of genotoxicity, cell toxicity and proteome profiling analysis. *Nanotoxicology* **2014**, *8*, 521–532. [CrossRef]
149. Schikorr, V.G. Uber Eisen(l1)-hydroxyd und ein lferromagnetisches Eisen(ll1)-hydroxyd. *Z. Anorg. Allg. Chem.* **1931**, *35*, 33–39.
150. Čakara, D.; Fras, L.; Bračič, M.; Kleinschek, K.S. Protonation behavior of cotton fabric with irreversibly adsorbed chitosan: A potentiometric titration study. *Carbohydr. Polym.* **2009**, *78*, 36–40. [CrossRef]
151. Dobaj Štiglic, A.; Kargl, R.; Beaumont, M.; Strauss, C.; Makuc, D.; Egger, D.; Plavec, J.; Rojas, O.J.; Stana Kleinschek, K.; Mohan, T. Influence of Charge and Heat on the Mechanical Properties of Scaffolds from Ionic Complexation of Chitosan and Carboxymethyl Cellulose. *ACS Biomater. Sci. Eng.* **2021**, *7*, 3618–3632. [CrossRef] [PubMed]